# National Laser Users' Facility and External Users' Programs

During FY03, the number of target shots dedicated to external users of OMEGA continued to increase as 733 target shots were provided. This represents 53% of the total target shots produced by OMEGA in the last year. External users' experiments were carried out by collaborative teams under the National Laser Users' Facility (NLUF) Program as well as by teams led by scientists from Lawrence Livermore National Laboratory (LLNL), Los Alamos National Laboratory (LANL), Sandia National Laboratory (SNL), and the Commissariat à l'Énergie Atomique (CEA) of France.

## FY03 NLUF Experiments

Seven of the nine NLUF programs approved in the last NLUF Review carried out a total of 123 target shots on OMEGA in FY03. Approved experimental NLUF Programs on OMEGA include the following:

***Experimental Astrophysics on the OMEGA Laser***
Principal Investigator: R. P. Drake (University of Michigan)

This project involves experiments in compressible hydrodynamics and radiation hydrodynamics, relevant to supernovae and supernova remnants. The experiments produce phenomena in the laboratory that are believed to be important to astrophysics but have not yet been directly observed in either the laboratory or in an astrophysical system. During FY03, the work focused on demonstrating techniques that can be used to explore the onset of turbulence in the three-dimensional, deeply nonlinear evolution of the Rayleigh–Taylor instability at a decelerating, embedded interface and on studies of collapsing radiative shocks. These experiments required strong compression and decompression, strong shocks (Mach ~10 or greater), flexible geometries, and very smooth laser beams, which means that the 60-beam OMEGA laser is the only facility capable of carrying out this program. During the past year, 2.5 shot days on OMEGA were allotted to this campaign, resulting in 25 target shots.

The exciting nature of this work has motivated the development of a collaborative effort that couples a core experimental team to theoretical groups at several institutions. Simulations guide the experimental planning to enable the acquisition of high-quality data and to provide for a comparison of several codes against the experimental data. Because they are complex and explore deep nonlinear effects, these experiments are excellent for verification and validation (V&V) of complex computer codes, including those produced by the ASCI Alliance Center at the University of Chicago. This program is also a critical steppingstone toward the use of the National Ignition Facility (NIF) both for fundamental astrophysics and as a critical component of ASCI V&V.

1. Development of Turbulence in Rayleigh–Taylor (RT) Instability at a Decelerating, Embedded Interface

As the scaling analysis in the paper by Robey *et al.*[1] indicates, it should be possible to observe the transition to a turbulent state in the evolution of the Rayleigh–Taylor instability that develops from a 3-D initial condition in the OMEGA experiments. Prior experiments on OMEGA indicated that several improvements in experimental technique were required to clearly observe the turbulent transition. During the past year, three such improvements were implemented:

a. An iodine-doped plastic that can be used for the tracer layers in the OMEGA targets was developed. Iodine has a higher x-ray opacity than the bromine that was used previously; this enhances the contrast of the x-ray images and extends the time over which the growth of the instabilities can be observed.

b. X-ray radiography using a backlit pinhole was implemented. Figure 96.47 shows the geometry of the initial targets using this technique. Laser beams irradiated a spot in the middle of the rear surface of a Ti foil, producing $K_\alpha$ x rays. Some of these x rays passed through a 10-$\mu$m pinhole in a Ta substrate, irradiating the target. A detector behind the target recorded the image. This technique produces much brighter images, and correspondingly improved signal-to-noise ratios, than the technique of area backlighting used previously.

c. A second x-ray-backlighting view of the target is being developed, which can look along the tracer strip (see Fig. 96.47). In this view, the strip itself is very opaque, but it will be possible to detect the lateral transport of material from the strip. The development of rapid lateral transport is a signature of the "mixing transition" that occurs with the onset of turbulence. In the initial attempt to implement the second view, the two views were not shielded well enough from one another. An improved design is currently being tested.

The first two improvements worked well and produced greatly improved data, as shown in Fig. 96.48. To demonstrate the improved techniques, targets with split perturbations were used: a single 2-D perturbation on half the interface (50-$\mu$m wavelength, 5-$\mu$m peak-to-valley amplitude) and a second, short-wavelength mode (5-$\mu$m wavelength, 0.5-$\mu$m peak-to-valley amplitude) on the other half. This provided worthwhile data regarding the effects of a second mode to compare with simulations. In addition, it is now possible to obtain reasonable-quality data as late as 37 ns after the start of the laser pulse, which is much later than could be obtained previously. Analysis continues, but the preliminary conclusion is that the second mode has a much smaller effect than is predicted by the simulations.

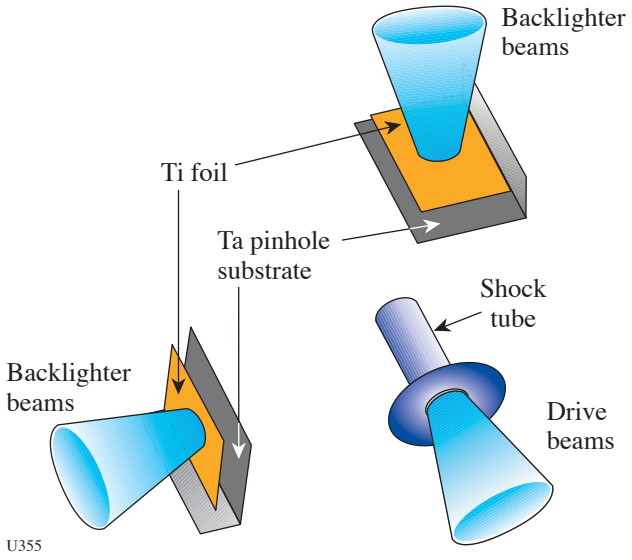


Figure 96.47
Target geometry for the Rayleigh–Taylor experiments using a backlit pinhole.

## 2. Collapsing Radiative Shocks

Astrophysical shocks, when they become cool enough, enter a radiatively collapsing phase in which their density can increase by several orders of magnitude. All supernova remnants eventually pass through this phase; blast waves emerging from supernovae pass through this phase, and such shocks arise in a number of other contexts. Using targets filled with xenon gas is expected to produce shocks that radiatively collapse on OMEGA. The goal is to produce such shocks, diagnose their properties, and study their evolution. This may include the development of structure due to the Vishniac instability.

Figure 96.49 shows a drawing of one of the targets that were used in these experiments. The laser beams irradiate the target from above, accelerating the thin (50 $\mu$m Be or 82 $\mu$m CH) solid layer to more than 150 km/s. This drives a shock down the tube, strong enough that it is predicted to collapse. The shock has been diagnosed using radiography (from left to right) or VISAR (through the lateral tubes). Simulations predict that x-ray radiographs should observe a collapsed xenon layer that is much narrower than the xenon layer that would be seen without the effects of radiation, as illustrated in Fig. 96.50.

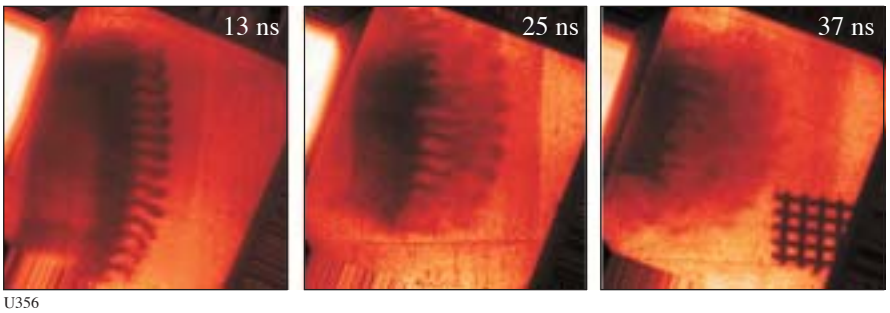


Figure 96.48
Radiographs using a backlit pinhole and an iodine-doped tracer layer.

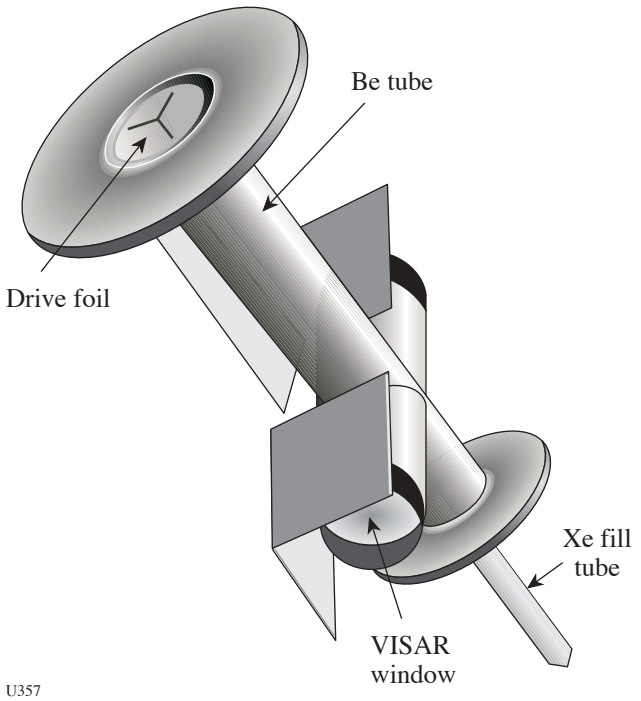


Figure 96.49
Drawing of a target used for radiative shock experiments.

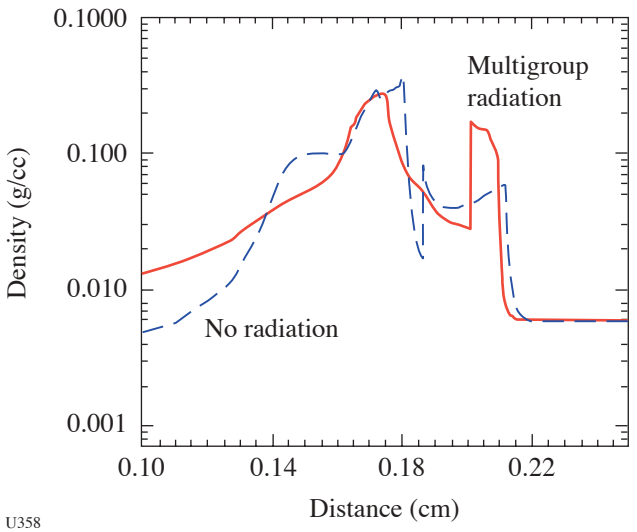


Figure 96.50
The effect of radiation should be to produce a thin, dense layer of xenon. The width of the layer in the simulation is just under 100 $\mu$m.

An actual radiograph, obtained using area backlighting, is shown in Fig. 96.51. A layer of xenon whose thickness is roughly consistent with the predictions of the simulation can be seen in this photograph. Since an improved signal-to-noise ratio is also required here, an attempt was made to employ a backlit pinhole for this application. Despite the similarity of the pinhole structure to those used previously with success, the specific pinhole design used for this experiment created shrapnel that damaged the imaging diagnostic. The next experiments will employ a modified backlit pinhole design; improved radiography is expected. The achievement of stronger shocks using a thinner initial layer, driven with SSD-smoothed laser beams, is also anticipated.

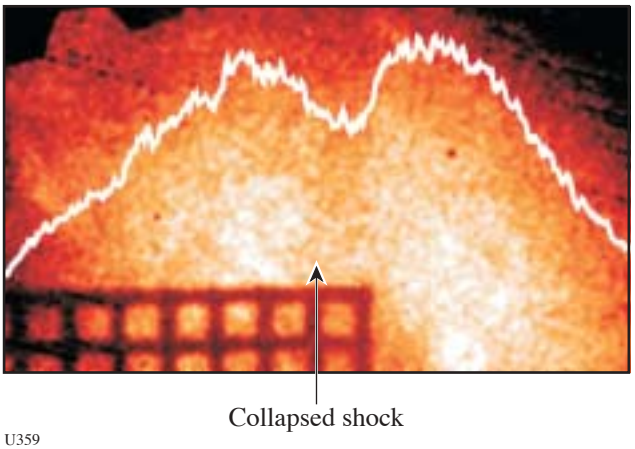


Figure 96.51
Radiograph of a shocked layer in xenon gas. The squares in the grid are 63 $\mu$m from wire center to wire center, so the observed layer is ~80 $\mu$m thick.

Several publications on experimental astrophysics were published by this group during the past year (see Refs. 1–5).

### *Optical-Mixing–Controlled Stimulated Scattering Instability V (OMC SSI V)*

Principal Investigator: B. B. Afeyan (Polymath Research Inc.)

The principal aim of this program is to investigate the evolution of backscattering instabilities of a witness beam in the presence of optical-mixing–generated plasma waves created by beating a blue pump beam with a green probe beam. This experiment was allotted 1.5 days of OMEGA time in FY03 and a total of 21 target shots were taken. In FY03, crossed blue- and green-beam experiments were conducted in exploding foil targets for the first time on OMEGA using a wide-enough DPP-generated spot so as not to be overwhelmed with excessive green-beam filamentation. A new phenomenon was observed that not only confirms that energy was success-

fully transferred from the blue beam to the green beam, but also confirms that a significant increase in the Raman backscattering of the green beam was triggered due to its interaction with the blue. A 15-fold increase in peak energy reflected by SRS (stimulated Raman scattering) was observed at an incident green-beam energy level of 100 J, while the crossing blue beam was at 500 J as compared to the same energy in green with the blue beam off as shown in Fig. 96.52. Figure 96.52(a) shows the SRS signal from the green beam alone, while Fig. 96.52(b) shows the backscattering of the green beam when the crossing blue beam is near 500 J. Figure 96.53 shows the same phenomenon for different target illumination conditions that gave rise to a hydrodynamic expansion that reached the necessary resonant density for energy transfer between the blue and green beams later in time and at colder temperatures. The same phenomenon is observed later in time, confirming the validity of the interpretation and the exceptional reproducibility of this instability energy transfer result, where incident blue-beam energy ends up becoming SRS-reflected energy from the green beam. This is a new wavelength conversion process where long wavelengths are produced by a controlled two-step process. It implies that the interpretation of the physics of laser–plasma interactions based on single interaction-beam experiments may be incomplete when extrapolated to predict the behavior of multiple beams crossing in a plasma. The results may not be strictly additive but highly nonlinear and multistep in nature. These new phenomena are being studied using parallel Vlasov–Maxwell simulations. Transmitted-beam diagnostics on the green probe beam confirm these findings by showing that the energy transfer from the blue to the green crossing beam was approximately a factor of 2.

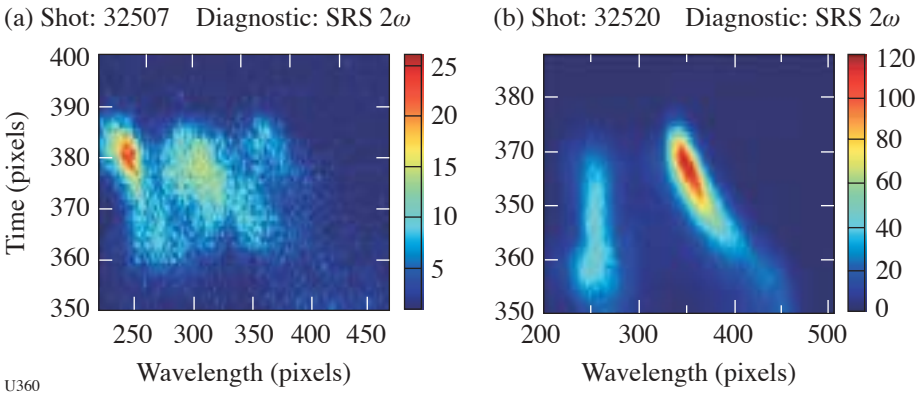


Figure 96.52
SRS reflectivity of a green beam in the absence (a) and presence (b) of a blue crossing beam. The peak reflectivity is increased by a factor of 15 or more when the signature of the peak of the exploding foil is considered (long-wavelength feature).

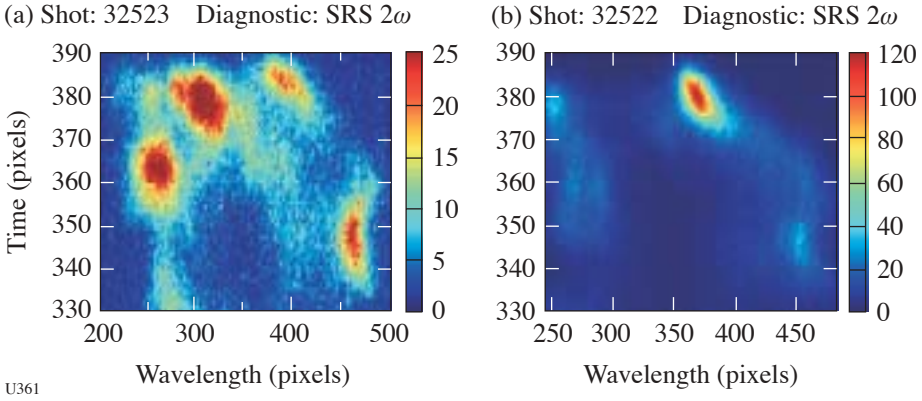


Figure 96.53
Same as Fig. 96.52 except that the plasma expansion is now delayed due to the elimination of two of the plasma heater beams. Note how Fig. 96.53(b) is very similar to Fig. 96.52(b) except for the time delay and subsequent reduction in the temporal extent of the green-beam SRS backscattering.

***Time Evolution of Capsule ρR and Proton Emission Imaging of Core Structure***

Prinicpal Investigator: R. D. Petrasso (Plasma Science and Fusion Center, MIT)

This program is aimed at the use of charged-particle measurements to address important issues in inertial confinement fusion (ICF) and high-energy-density physics. During FY03, 1.5 OMEGA shot days were allotted to this program, and 18 target shots were taken. The experiments were in two main areas: proton core imaging and studies of $\rho R$ asymmetry growth.

1. Proton Core Imaging Spectroscopy (PCIS) for OMEGA Implosions

Penumbral proton imaging was used to study the spatial distributions of DD and $D^3He$ reactions in imploded $D^3He$-filled capsules on OMEGA.[6,7] The imaging was performed with a pinhole camera in which the recorder consisted of stacked sheets of CR-39 nuclear track detector separated by ranging filters, which resulted in efficient detection of 14.7-MeV $D^3He$ protons on one sheet [see Fig. 96.54(a)] and 3-MeV DD protons on another. Measurements of the nuclear burn region are important for investigating the extent of the burn, the presence of burn asymmetries, the effects of mix and thermal conduction on the burn region, and the accuracy of code predictions. When target capsules have thin shells (e.g., 1.8 $\mu$m $SiO_2$), allowing both proton types to escape at burn time, the images on separate sheets of CR-39 can be used to reconstruct simultaneous radial profiles of DD and $D^3He$ burn. These can in turn be used to determine the fuel ion temperature ($T_i$; see Fig. 96.54) and the density ($n_i$). When capsules have thick shells (e.g., 20 $\mu$m CH), only the 14.7-MeV proton can escape through the capsule $\rho R$ at bang time and the measured $D^3He$ burn profile reflects the effects of compression and mix; but DD protons do escape at the earlier time of first shock coalescence, when $\rho R$ is far below its peak value, and the DD burn profile at that time can be studied. Since mix has been experimentally shown to be inconsequential at this instant, mean-ingful comparisons of 1-D simulations with experiments can be made.

2. Studies of $\rho R$ Asymmetry Growth Rates and the Relationship Between Laser Drive Asymmetry and $\rho R$ Asymmetry

During 2003, a series of shots were undertaken to study the implications of laser drive asymmetry for implosion dynamics and capsule performance, and several important conclusions were drawn from the resultant data. The series included six implosions of room-temperature capsules with 26-$\mu$m-thick CH shells and 18 atm of $D^3He$ gas fill, using 60 laser beams with full beam smoothing and ~23 kJ of total laser energy. Illumination asymmetry was introduced in a controlled way by offsetting the capsules from target chamber center (TCC) by specific amounts, resulting in deviations of the on-target laser intensity $\delta I(\phi)$ from the mean $\langle I \rangle$ that are dominated by mode numbers 1 and 2. Diagnostics used to record crucial data included six wedged-range-filter (WRF) proton spectrometers, the proton temporal diagnostic (PTD), x-ray framing cameras, pinhole cameras, and the GMXI framing camera. Figure 96.55 illustrates sample proton spectra recorded during implosions with three different target offset amounts, showing how the spectra are dramatically different at different angles and for different offsets. Each spectrum can be decomposed into two parts representing proton emissions at the time of first shock coalescence and at bang time (these times occur roughly 1.7 and 2.1 ns after the onset of the 1-ns laser pulse, respectively).

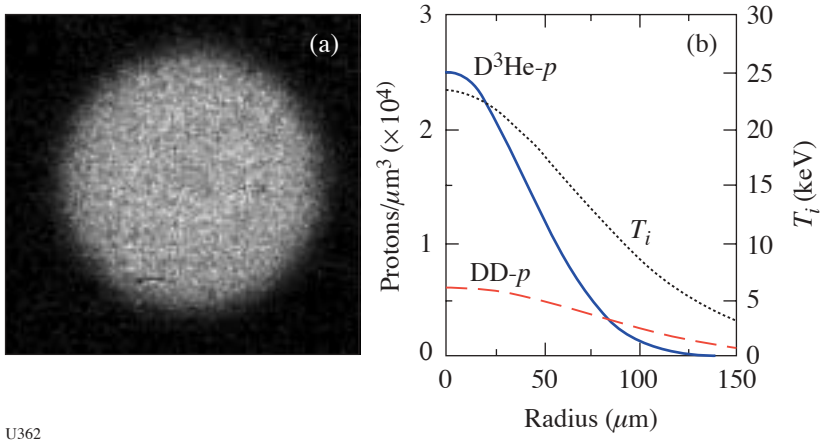


U362

Figure 96.54
PCIS data from OMEGA shot 27456, in which the capsule consisted of 18 atm of $D^3He$ in a 1.8-$\mu$m $SiO_2$ shell. (a) An image of $D^3He$ protons made behind a 600-$\mu$m-diam pinhole. Since the pinhole is much larger than the compressed capsule, all structural information is contained in the penumbra. (b) Radial profiles of proton emissivity in the imploded capsule, inferred from five pinhole images of $D^3He$ protons and five pinhole images of DD protons. Since the local ratio of the two reaction rates is a function of ion temperature $T_i$, the radial profile $T_i(r)$ can be inferred.

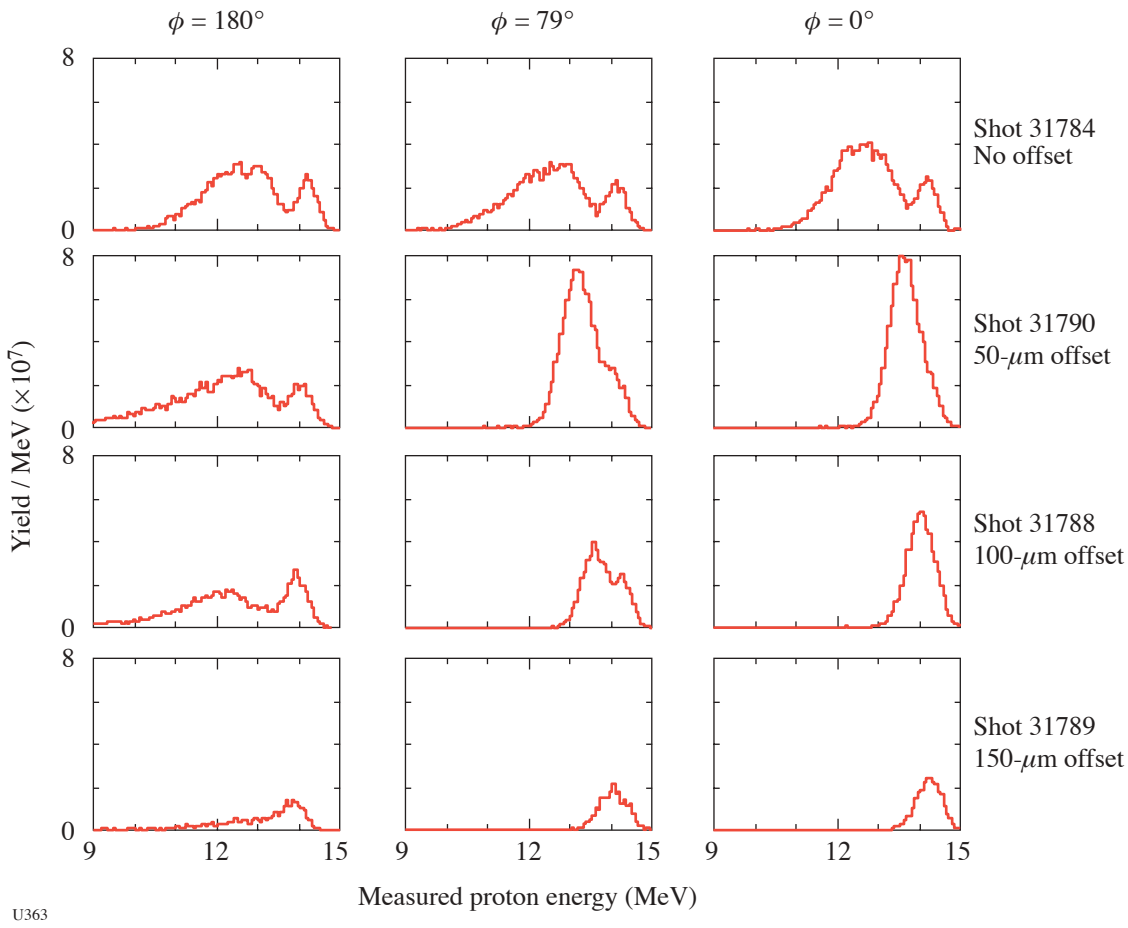


Figure 96.55
Proton spectra recorded at three important angles with respect to the direction of offset of the capsule from target chamber center. Offsets produce an asymmetric laser drive intensity on the capsule surface, with the maximum value at 180° and the minimum at 0° (see Fig. 96.56 for an example). With no offset, the spectra are all very similar, indicating an implosion that was quite symmetric. As the offset gets larger, $\rho R$ asymmetries get progressively larger and the size of the lower-energy peak (due to emission at compression time) becomes progressively smaller while the shock-time peak maintains a relatively constant size (see Fig. 96.57).

The energy spectra of the $D^3He$ protons were used to characterize the areal density ($\rho R$) as a function of angle at shock time and at bang time using spectrometers at different angles. It was found that the angular shape of the drive asymmetries is imposed on the $\rho R$ variations and maintained with no phase change through shock and bang times, as shown in Fig. 96.56. The growth in amplitude was roughly consistent with that recently predicted for Bell-Plesset–like convergence effects.[8] At each time, $\delta\rho R(\phi)/\langle\rho R\rangle \approx 0.4(C_r - 1)\delta I(\phi)/\langle I\rangle$, where $C_r$ is the radial compression ratio at that time and $\delta I(\phi)/\langle I\rangle$ is averaged over the laser pulse. The mean $\rho R$ at each time can also be used to estimate $C_r$, which turns out to be essentially independent of offset at shock time but a decreasing function of offset at compression time.

Considering the fuel, the data provide information about the dynamics of shock coalescence and the state of the fuel at bang time. The character of the shock coalescence is particularly important because simulations predict that asymmetrically launched shocks will not coalesce coherently enough to heat the hot spot. It was found in the experiments that, although the shock coalescence for offset targets was smeared out in time and space, the number of $D^3He$ protons emitted at this time was less sensitive to drive asymmetry than expected (Fig. 96.57). In fact, simulations had indicated that there would be no shock yield at all for the largest capsule offsets used. The yield at bang time, on the other hand, did diminish with increasing offset. This is qualitatively consistent with the finding from the $\rho R$ studies that the radial compression ratio decreased with increasing illumination asymmetry.

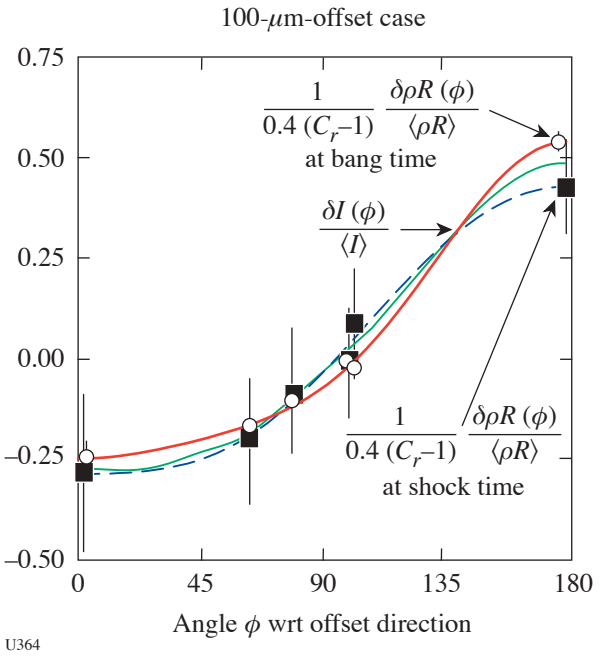


Figure 96.56
For an offset target implosion, the angular distribution of the measured $\rho R$ is similar at different times during the implosion.

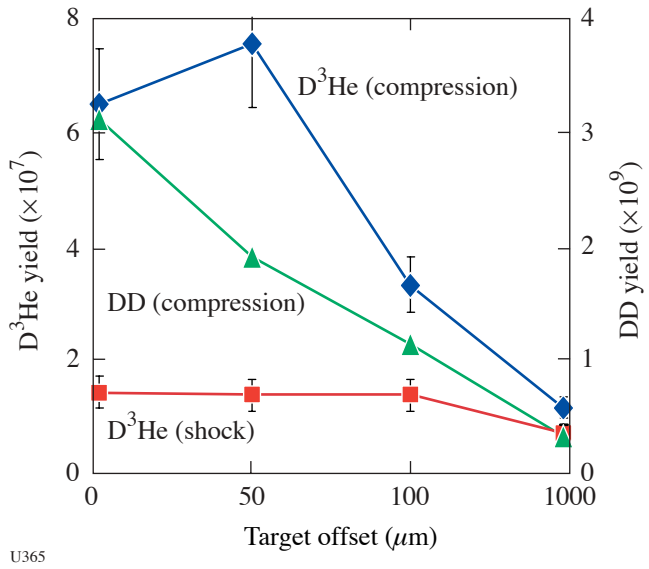


Figure 96.57
$D^3He$ and DD proton yields as a function of the offset of targets from TCC. Despite the smearing of the shock coalescence in space and time, the $D^3He$ proton yield at shock time remains largely unaffected by the drive asymmetry caused by target offset, while the yield at compression time decreases with offset.

### *OMEGA Laser Studies of the Interaction of Supernova Blast Waves with Interstellar Clouds*

Principal Investigator: C. McKee (University of California, Berkeley)

The objective of this experiment is to conduct experiments on OMEGA to (1) explore the role of turbulence in laser–target interactions and (2) study the laboratory analog of astrophysical "mass-loaded flows." The current experiments involve the interaction of strong shocks with single and multiple dense clumps embedded in a low-density inter-clump background.

By varying the composition and size of the target, the investigators were able to systematically vary the Reynolds number (Re) of the flow and study the onset of turbulence in a compressible flow. These experiments are relevant to astrophysical flows in which powerful shock waves produced by supernovae, stellar winds, and other phenomena propagate through an inhomogeneous medium. Mass is stripped from clouds and injected into the low-density, generally hot, intercloud medium—a phenomenon known as mass loading. These experiments specifically address the question of how the mass loading is affected by the Re of the flow. It is possible to determine whether there are significant changes in the mass and momentum exchange between the cloud and the intercloud medium at Re higher than those accessible to direct numerical simulation (the limit on numerical simulations is typically $\mathrm{Re} < 10^3$). A specific goal of the investigation is to find evidence for the transition from a vortex sheet to a turbulent wake; this appears at $\mathrm{Re} \sim 2 \times 10^4$ in compressible flow experiments. During this first year of the study, a single dense clump (sphere) is used; future work may extend this research to the case of multiple clumps. The results of the experiments will be compared with both 2-D and 3-D direct numerical simulations using adaptive mesh refinement.

During FY03, 1.5 shot days were allocated for these studies, and 14 target shots were taken. The experiments for this first year were directed to demonstrating a clearly diagnosable transition to a turbulent flow, which the investigators believe may look like that observed in incompressible experiments. Side-on and face-on radiographic images of reasonably high quality at 5 ns (face-on only), 12 ns, 19 ns, and 26 ns were obtained. Figure 96.58 shows side-on radiographic images that display the evolution of the shocked spherical cloud at 12 ns, 19 ns, and 26 ns. At 12 ns, the shock has just passed over the cloud, and the spherical cloud displays a symmetrical extension in the axial direction with the start of a Kelvin–Helmholtz rollup of the sides of the cloud. By 19 ns, corresponding to 6.7

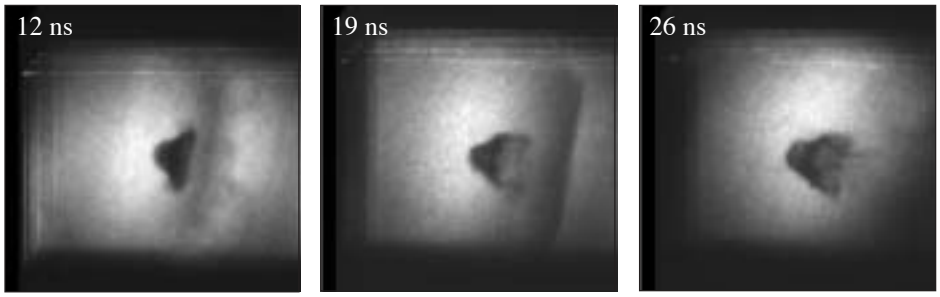


U366

Figure 96.58
X-ray radiographic images of the interaction of a strong shock wave with a spherical object. The sphere is initially 120 $\mu$m in diameter and located 500 $\mu$m from the ablative surface of a 1500-$\mu$m-diam cylindrical shock tube. (The side of each square image is approximately 1150 $\mu$m.)

crushing times, the face-on images (not shown) display the initial development of the vortex-ring instability predicted and observed in earlier work on Nova and OMEGA.[9,10] The basic symmetry of the shocked sphere seen in the side-on radiograph indicates that the flow is most likely still laminar. At 26 ns, corresponding to 9.8 crushing times, nonaxisymmetric flow is clearly evident in the side-on radiographs with evidence of asymmetric jetting and strong Kelvin–Helmholtz instabilities. This is most likely the start of strong vortex-ring instabilities and the transition to turbulent flow. Two-dimensional simulations to model the shock–sphere interaction have been conducted. Later time evolution of the interaction will require detailed 3-D AMR simulations that will also be performed.

***High-Spatial-Resolution Neutron Imaging of Inertial Fusion Target Plasmas Using Neutron Bubble Detectors***
Principal Investigaor: R. K. Fisher (General Atomics)

The goal of this research is to develop techniques to record the bubble spatial distribution in a high-efficiency liquid bubble chamber that may have potential use for NIF neutron imaging. This program had only limited funds and no dedicated shots in FY03. Its focus was the study of alternative bubble-recording techniques, including light scattering and x-ray transmission, with the goal of determining the most-promising method prior to initiating laboratory tests.

An initial assessment of x-ray transmission was carried out, and the following potential advantages of this approach were identified:

– a change in x-ray transmission allows measurements under expected NIF conditions since there will be many bubbles behind bubbles;

– the photoelectric effect dominates x-ray attenuation and minimizes the multiple scattering "crosstalk" issue inherent in light-scattering approaches;

– bubble-distribution measurements should be allowed over a wide range of NIF *n*-yields; flash x-ray timing can be chosen to optimize bubble radius and, therefore, $\Delta(\rho x)$ along x-ray paths.

1. Future Plans

- Complete preliminary assessment of x-ray and light-scattering approaches to bubble distribution measurements.

- Perform laboratory tests to address important issues, e.g., the effects of multiple scattering during light scattering/transmission measurements.

- Prepare for system tests/neutron-imaging experiments to test bubble chamber and readout techniques on OMEGA in FY05 and later.

  – The bubble chamber used will depend on the status of LLE and Russian research on bubble detector development for neutron imaging.

***Dynamic X-Ray Diffraction of Shocked Single Crystals***
Principal Investigator: M. Meyers (University of California, San Diego)

The NLUF x-ray-diffraction project focused on two separate goals: (1) to use the *in-situ* diffraction technique to study the response of a single-crystal lattice to shock loading, and (2) to characterize the deformation mechanisms in metals by shocked-sample recovery and electron microscopy. During FY03, two days of OMEGA shot time were allocated to this project, and 21 target shots were taken.

The *in-situ* diffraction technique provides a direct measurement of the lattice response under shock loading. It may be used to characterize a solid–solid phase transition such as the bcc–hcp transition in iron. The configuration for the diffraction

experiments was modified to use a different shock drive beam incident on the same side of the sample as the x-ray-diffraction probe in order to be able to hold the sample under compression for a longer time during the diffraction measurement. This modified geometry is shown in Fig. 96.59.

Recovery experiments provide a simple way to examine the deformation mechanisms governing high-strain-rate phenomena. By examining the residual microstructure and defect substructure with advanced analytical tools like transmission electron microscopy, the mechanisms in operation during shock loading can be inferred. The goal of these recent experiments is to probe the transition between the mechanisms of slip and twinning in single-crystal copper and copper–aluminum alloys in terms of composition, pressure, and orientation. Figure 96.60 shows micrographs of copper 2 wt% aluminum shot with laser energies of 200 J, which correlates to a peak pressure of 40 GPa. In the first image [Fig. 96.60(a)], the orientation is [001] and four twinning variants are observed. The second image [Fig. 96.60(b)] is the orientation $[\bar{1}34]$ revealing two sets of microtwins.

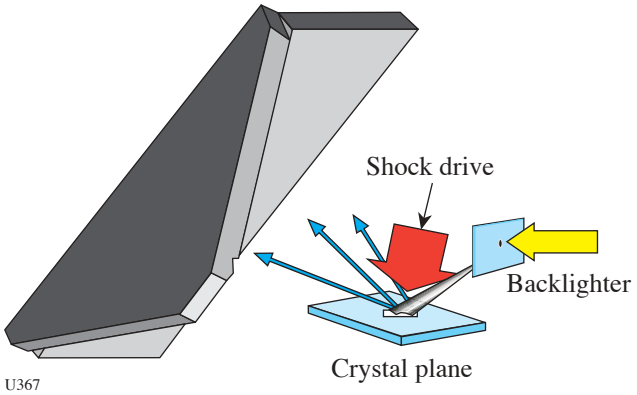


Figure 96.59
Schematic illustrating the geometry of the dynamic x-ray-diffraction experiment.

### *Study of Driven Ion-Acoustic Waves Under Direct-Drive Conditions*

Principal Investigator: H. Baldis (University of California, Davis)

The aim of this program is to study the physics of laser interactions with ion-acoustic waves (IAW's) in plasmas at conditions relevant to direct-drive inertial confinement fusion (ICF) targets on the National Ignition Facility (NIF). Though no OMEGA shots were scheduled for this program in FY03, good progress was made on the understanding of the seeding of stimulated Brillouin scattering (SBS) by a number of effects. In direct-drive ICF geometry, many laser beams overlap with different angles of incidence, at any point over the capsule. In the plasma corona surrounding the capsules, this leads to a number of wave–wave coupling configurations, which modify the initial growth of the SBS instability. Preliminary studies have been carried out, both theoretical and experimental, on the effect of reflection of laser light and forward-scattered light from the critical density, as well the effect of seeding by side-scattered SBS light from adjacent beams.

The shots allocated to this project on OMEGA in FY04 will be dedicated to experiments to characterize some of these seeding mechanisms. The recently incorporated Thomson-scattering diagnostic will be used, at $4\omega$, to study the amplitude and saturation of IAW's associated with SBS. An important component will be the identification of seeding of the instability, by either sidescattering from adjacent beams or reflection

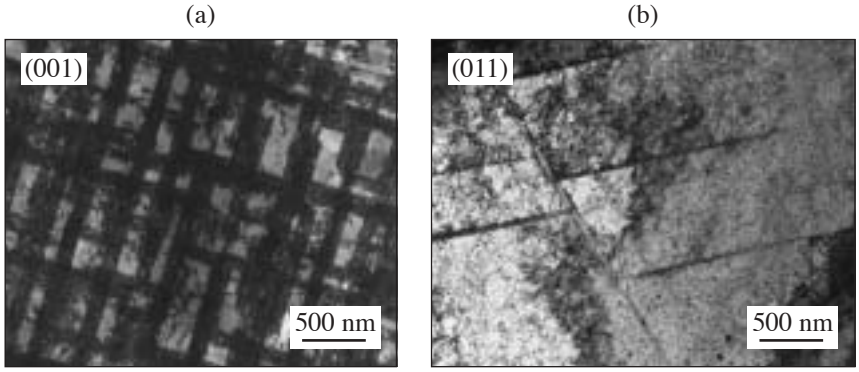


Figure 96.60
Transmission electron micrographs of a copper (2-wt%) aluminum sample irradiated with 200 J in a 2.5-ns pulse. The peak pressure in these samples was 40 GPa. (a) In copper (2-wt%) aluminum oriented to [001], four twin variants are observable at a high density; (b) in copper (2-wt%) aluminum oriented to $[\bar{1}34]$, two twinning variants are observable in considerably lower densities.

of laser light from the critical density. In past experiments the nonlinear coupling from different beams has been observed using the backscattered light as a diagnostic.[11]

***Experimental and Modeling Studies of 2-D Core Gradients in OMEGA Implosions***

Principal Investigator: R. C. Mancini (University of Nevada, Reno)

The objective of this program is to determine the spatially and temporally resolved two-dimensional (2-D) temperature and density core gradients of high-energy-density plasmas arising from OMEGA implosions. During the first year of the project substantial progress was made in the areas of instrument development, experiments, and data analysis.[12,13] One full OMEGA shot day was allocated, and nine shots were taken for this program. Two multi-monochromatic-imager (MMI) instruments were built and successfully fielded in indirect-drive implosion experiments on OMEGA. The plastic shells used in the experiments were filled with deuterium and doped with a tracer amount of argon for diagnostic purposes. The first imager operates in time-integration mode, while the second one records time-resolved images. For this second instrument, new (more-efficient) multilayer mirrors were designed and fabricated as well. With the availability of these additional instruments, simultaneous (i.e., in the same shot) recording of two sets of narrowband x-ray images of the core along two quasi-orthogonal directions perpendicular to the hohlraum axis is possible. This capability is critical for extracting information about the 2-D/3-D space structure of the core. A third imager has been tested in an effort to record a third set of narrowband images along a direction parallel to the hohlraum axis. Two series of five shots each were performed during FY03. In the first series, three types of beam pointing were tested that led to the production of round, "mild-sausage," and "sausage" implosion cores with a major axis along the hohlraum axis. In this way, it has been shown that a sequence of implosion cores can be produced where 2-D spatial structure effects are gradually "turned on." Processing the image data recorded in these implosions allowed the construction of 2-D emissivity maps associated to the argon $He_\beta$ and $Ly_\beta$ lines. Since the $Ly_\beta$ to $He_\beta$ emissivity ratio is a strong function of the temp-erature and a weak function of the density, $Ly_\beta/He_\beta$ emissivity ratio maps were used to compute 2-D temperature maps of the core. Furthermore, 2-D scaled maps of the density were also obtained. Temperature and density maps show significant changes depending on the type of core, i.e., round, mild sausage, or sausage. In the second series of shots, time-resolved images were recorded.

The capsules used in both FY03 shot series were plastic shells filled with 50 atm of deuterium and doped with 0.1 atm of argon for spectroscopic diagnostic purposes. In addition to the x-ray imagers, time-resolved, space-integrated, argon *K*-shell x-ray line spectra were also recorded with the streaked SSCA or SSC1 crystal spectrometers in all shots. The line of sight (LOS) for these instruments was always through a laser entrance hole (LEH).

On the first series of shots, the focus was to record time-integrated images along two quasi-orthogonal directions close to the hohlraum midplane. In addition, a standard framing camera (XRFC2) was used to look at the implosion core down the hohlraum axis. A reference case of beam-pointing parameters was used to obtain round implosions (established in the team's previous NLUF project), and then the beams gradually moved (both cones, 2 and 3) in two steps of 30 $\mu$m each with the goal of driving mild-sausage and sausage implosion cores, i.e., ovals of gradually increasing eccentricity, with the major axis along the hohlraum axis. The results of the analysis clearly show the changes in core symmetry and spatial structure of the temperature and density distribution.

In the second shot series, the goal was to record time-correlated images and spectra with time resolution. Beam pointing was set to the reference case of round cores. MMI-3a (from the team's earlier NLUF project) and MMI-3b were mounted in TIM-2 and TIM-3, respectively, and SXRFC was mounted in TIM-4 (an SSCA was mounted in TIM-6); therefore, TIM-2, TIM-3, and TIM-4 defined a system of quasi-orthogonal *x*-*y*-*z* axes for these shots. Time-resolved data were successfully recorded with MMI-3b.

Progress in data analysis in FY03 focused on improving the capability of performing 1-D core gradient determination in round cores, and, in the first step, on developing and testing methods for extracting 2-D temperature and density spatial gradients from image data.

Figure 96.61 shows the results of 1-D core gradient determination for a round core. The gradients were extracted using a gradient reconstruction method that searches the parameter space of gradient functions with the goals of simultaneously and self-consistently fitting the spatial emissivity profile of the argon $He_\beta$ line emission (obtained from a narrowband x-ray image) and the space-integrated argon line spectra covering the spectral range of the $He_\beta$, $He_\gamma$, and $Ly_\beta$ lines and their associated Li- and He-like satellite transitions (i.e., multi-objective data analysis). The search in parameter space is

driven by a novel application of a niched-Pareto genetic algorithm (NPGA) to plasma spectroscopy. This algorithm is actually general and can be applied to other problems of multi-objective data analysis. The error bars are determined by taking into account solutions found in the vicinity of the optimal one, and by repeating the analysis for the same case considering the angle dependence of emissivity profiles, i.e., accounting for deviations from perfect spherical symmetry. Gradient uncertainties due to these effects are then added in quadrature. The consistency of these gradients with the emissivity spatial profile extracted from the analysis of the $Ly_\beta$ image was also checked. Thus, these gradients are effectively constrained by three criteria: $He_\beta$ and $Ly_\beta$ emissivity spatial distributions and space-integrated line spectrum. Testing this capability in 1-D cases is important before extending them for application in 2-D problems.

An alternative method for temperature determination is based on the fact that the $Ly_\beta/He_\beta$ emissivity ratio is a strong function of the temperature and a weak function of the density. Therefore, a space map of this emissivity ratio obtained by processing core image data can be directly transformed point by point into a space map of temperature. The temperature gradient determined by this method showed good consistency with the result obtained via the gradient reconstruction method.

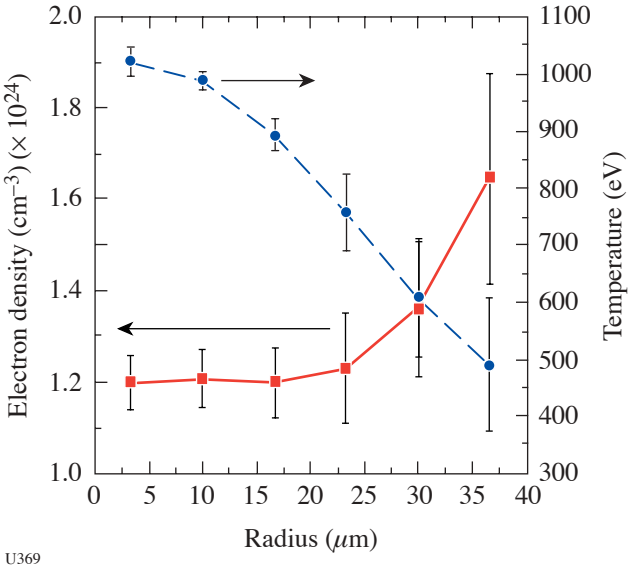


Figure 96.61
Results of 1-D core gradient reconstruction for OMEGA shot 26787.

In a first step toward determining the spatial distribution of temperature in the core beyond the 1-D approximation, the emissivity ratio method described in the previous paragraph was applied to the analysis of the image data recorded in the December 2002 shots. On shots 29885, 29889, and 29890, round, mild-sausage, and sausage cores were created intentionally (by adjusting the beam pointing) with the major axis along the hohlraum axis. Considering core slices cut perpendicular to the hohlraum axis and assuming axial symmetry (locally) in each slice, emissivity profiles in the core can be obtained from the $He_\beta$ and $Ly_\beta$ image data. This procedure can be interpreted as a generalized Abel inversion. Next, the $Ly_\beta/He_\beta$ emissivity ratio maps were interpreted and directly converted into 2-D (actually, quasi-3-D) spatial maps of core temperature. Results obtained for these three shots are displayed in Figs. 96.62–96.64. The hohlraum axis is along the vertical direction. The characteristic size of these implosion cores is 60 to 80 $\mu$m. Changes in core symmetry and temperature spatial distribution are apparent from the maps.

After the temperature map has been determined, scaled density maps can be obtained by working separately with each line emissivity map ($He_\beta$ or $Ly_\beta$) and solving point by point for the density given the local values of emissivity and temperature. These results are also shown in Figs. 96.62–96.64. Note that the density maps extracted from the $He_\beta$ emissivity are not identical to those extracted using the $Ly_\beta$ emissivity; however, they are very similar, suggesting that the process is sound. Again, changes are observed from round to sausage cores. In particular, a two-peak density (and temperature) spatial structure develops for the mild-sausage and sausage implosion cores along the major axis.

Finally, Fig. 96.65 shows the time-resolved data obtained in OMEGA shot 31594 (May 2003) with MMI-3b. Round-core beam pointing was used in this shot. Each frame is characteristic of a 50-ps time interval and displays simultaneous core images and a slit spectrum. Both images and spectra data show significant changes as a function of time that are being used to study the time evolution of the core's spatial structure. Work is in progress in the analysis of these data.

FY04 will focus on (1) obtaining time-resolved data for studying the 2-D spatial structure of round, mild-sausage, and sausage implosion cores, (2) contining work on alternative generalized Abel-inversion procedures, (3) applying 2-D gradient reconstruction methods to determine the spatial structure of implosion cores, and (4) performing detailed comparisons between data analysis and hydrodynamic simulation results.

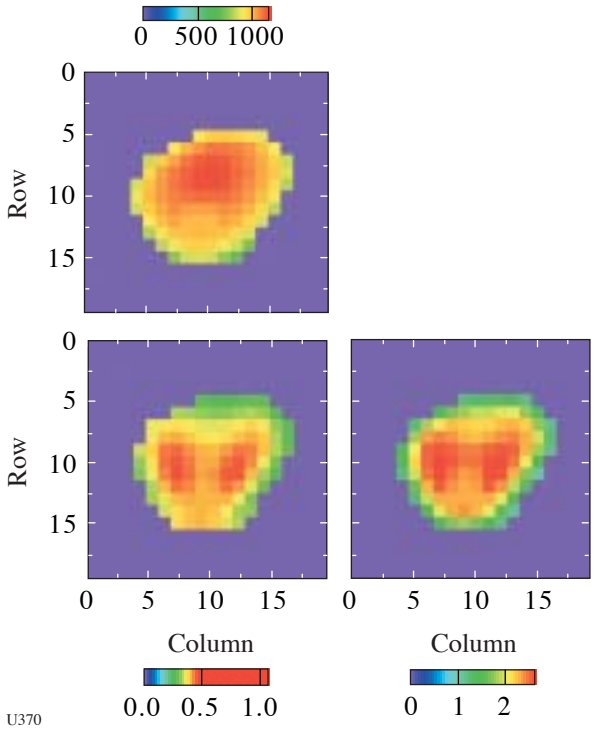


Figure 96.62
Time-integrated 2-D electron temperature (top, in eV) and scaled electron-density maps (bottom, in units of $1 \times 10^{24}$ cm$^{-3}$) for OMEGA shot 29885, round implosion core case. Electron-density maps (left) based on He$_\beta$ emissivity and (right) based on Ly$_\beta$ emissivity.

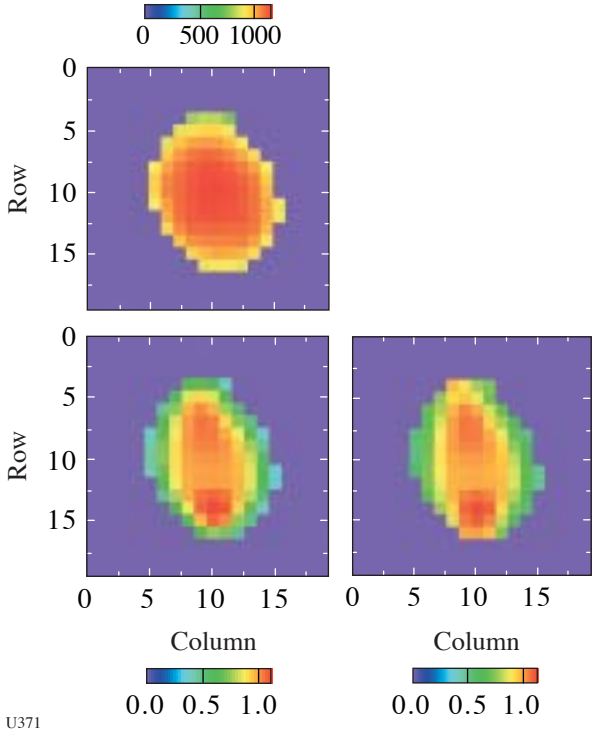


Figure 96.63
Time-integrated 2-D electron temperature (top, in eV) and scaled electron-density maps (bottom, in units of $1 \times 10^{24}$ cm$^{-3}$) for OMEGA shot 29889, mild-sausage implosion core case. Electron-density maps (left) based on He$_\beta$ emissivity and (right) based on Ly$_\beta$ emissivity.

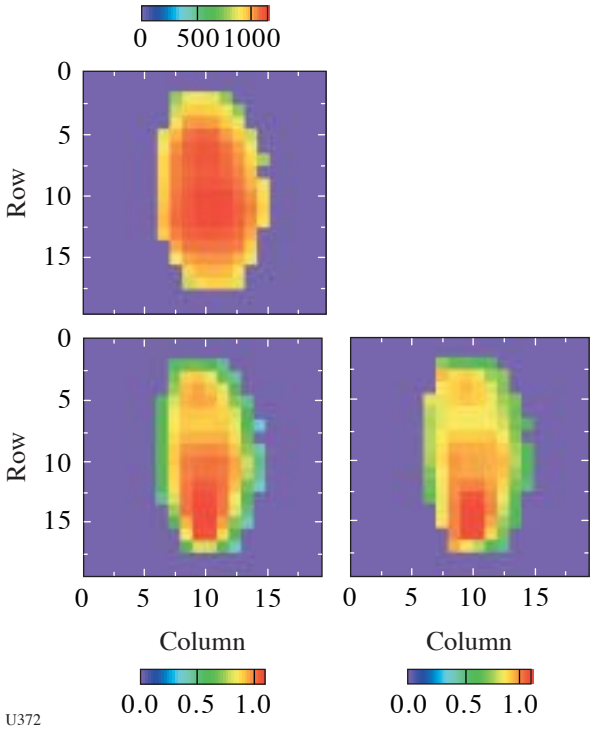


Figure 96.64
Time-integrated 2-D electron temperature (top, in eV) and scaled electron-density maps (bottom, in units of $1 \times 10^{24}$ cm$^{-3}$) for OMEGA shot 29890, sausage implosion core case. Electron-density map (left) based on He$_\beta$ emissivity and (right) based on Ly$_\beta$ emissivity.

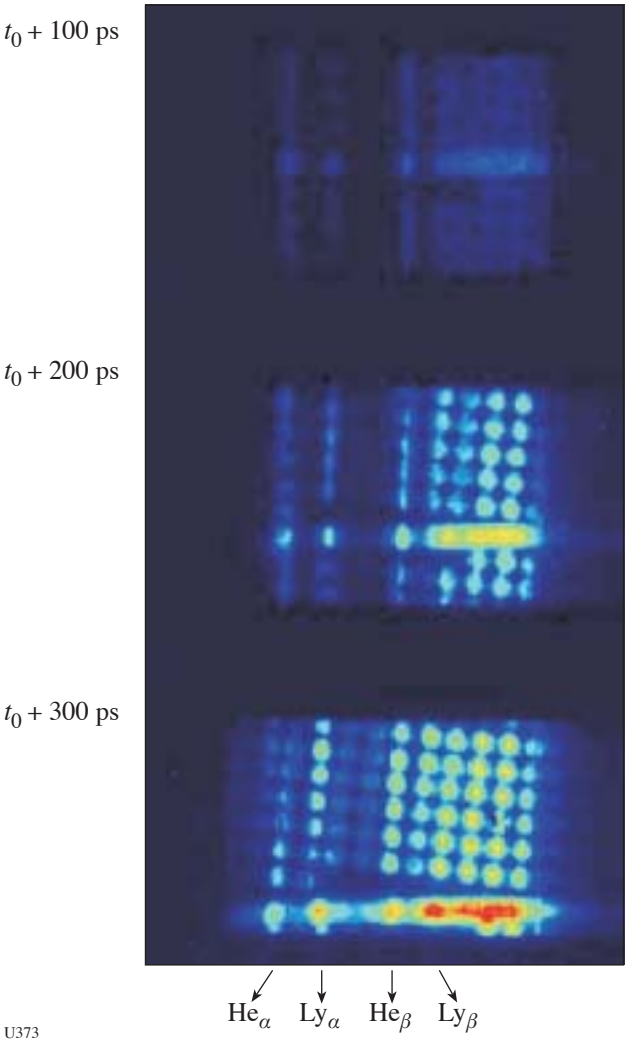


Figure 96.65
Time-resolved core images and slit spectrum recorded in OMEGA shot 31594 with MMI-3b.

### *Recreating Planetary Core Conditions on OMEGA: Techniques to Produce Dense States of Matter*

Principal Investigator: R. Jeanloz (University of California, Berkeley)

The objective of this program is to use OMEGA to determine the nature of planetary fluids at the extreme conditions representative of the cores of the giant planets. To achieve the required conditions, this team has developed diamond anvil cell (DAC) targets for laser shock-compression experiments. With this technique the initial sample pressure is much higher than ambient (3 to 20 kbar), and the initial density may be from 1.5 to 5 times higher than ambient (depending on the sample) compared to nonpressurized preparation methods. The higher initial density results in a significantly larger final density and lower temperature in the shock-compressed state. Single- and multiple-shock Hugoniot techniques of precompressed targets can re-create deep interior states of giant solar planets, extrasolar planets, and low-mass stars.

In FY03, 1.5 shot days were allotted to this program, and 15 target shots were performed on precompressed samples (hydrogen, helium, and nitrogen ) on the OMEGA laser. As shown in Fig. 96.66, a thin (≤200-$\mu$m) drive diamond was laser-ablated to send a shock through the sample (~100 $\mu$m thick) loaded in a DAC. The primary diagnostic was the velocity interferometer system for any reflector (VISAR). Table 96.VII lists the first ten target shots of FY03.

Highlights of the experiments are shown in Fig. 96.67, which shows the results of shot #31455: helium precompressed to 5.5 kbar. The sample remained transparent with a particle velocity of approximately 2 $\mu$m/ns. (It is likely that the laser was misaligned and the observed pressure was much lower than expected based on the incident energy.) Figure 96.68 shows the results for shot #30758: helium precompressed to 2.7 kbar. As in three other shots, one can see the shock breakout into the helium sample but the helium was nontransparent. Figure 96.69 shows the results for shot #30759: hydrogen precompressed to 3.6 kbar. The sample was nontransparent (transparent at the edges, where edge rarefaction has sufficiently lowered the pressure). At times after breakout of about 8 and 12 ns, re-shock and rattling of the shock into a more-reflective state were observed. The pressure of this shock is estimated to have been about 420 kbar with a re-shock pressure

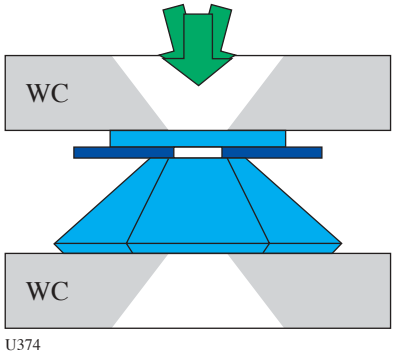


Figure 96.66
Illustration of diamond anvil cell (DAC) geometry. Tungsten carbide (WC) is used as a support for the DAC.

of about 1.1 Mbar. Figure 96.70 shows the results of shot #31457: nitrogen precompressed to 5.2 kbar. In this shot the nitrogen shock was reflecting, showing a strong decay in shock velocity from about 24 to 19 $\mu$m/ns. When the shock hit the back diamond, the VISAR fringes suddenly disappeared due to the diamond window going opaque (consistent with a diamond shock pressure above about 1.5 Mbar). The spatial extent of the shock reflectivity implied that the radius of curvature in this shot was 300 to 400 $\mu$m, consistent with the use of 300-$\mu$m phase plates.

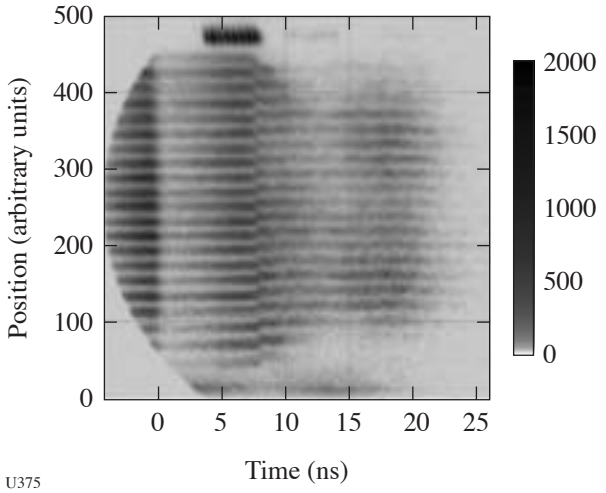


Figure 96.67
VISAR data from shot #31455: He precompressed to 5.5 kbar.

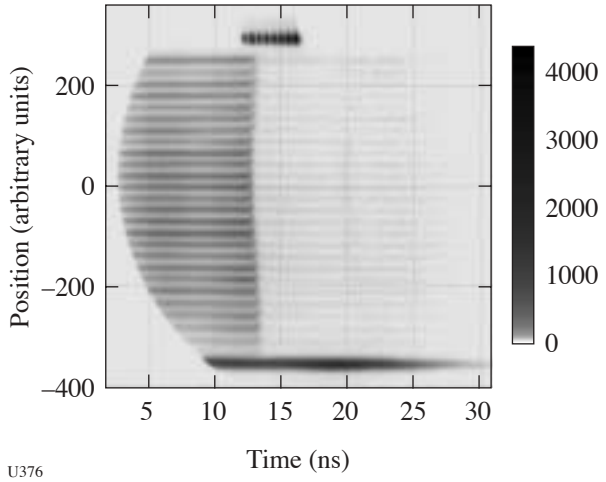


Figure 96.68
VISAR results from shot #30758: He precompressed to 2.7 kbar.

Table 96.VII: Target shots to explore planetary core conditions on OMEGA—the first ten shots of FY03.

| LLE Shot # | Sample | Initial Pressure (kbar) | Initial Density (g/cc) | Laser Intensity ($W/cm^2$) | Results |
|---|---|---|---|---|---|
| 30755 | He | 5.4 | 0.301 | $6.5 \times 10^{14}$ | Opaque diamond |
| 30756 | He | 5.4 | 0.301 | $5.2 \times 10^{14}$ | Opaque diamond |
| 30757 | Surrogate | — | — | $5.2 \times 10^{14}$ | — |
| 30758 | He | 2.7 | 0.211 | $5.1 \times 10^{13}$ | Nontransparent |
| 30759 | $H_2$ | 3.6 | 0.127 | $4.5 \times 10^{13}$ | Nontransparent |
| 31454 | He | 1.6 | 0.154 | $5.3 \times 10^{14}$ | Nontransparent |
| 31455 | He | 5.5 | 0.304 | $2.7 \times 10^{14}$ | Transparent |
| 31456 | $H_2$ | 6.2 | 0.142 | $2.7 \times 10^{14}$ | Nontransparent |
| 31457 | $N_2$ | 5.2 | 0.935 | $4.1 \times 10^{14}$ | Reflecting |
| 31459 | He | 5.9 | 0.314 | $2.6 \times 10^{14}$ | Nontransparent |

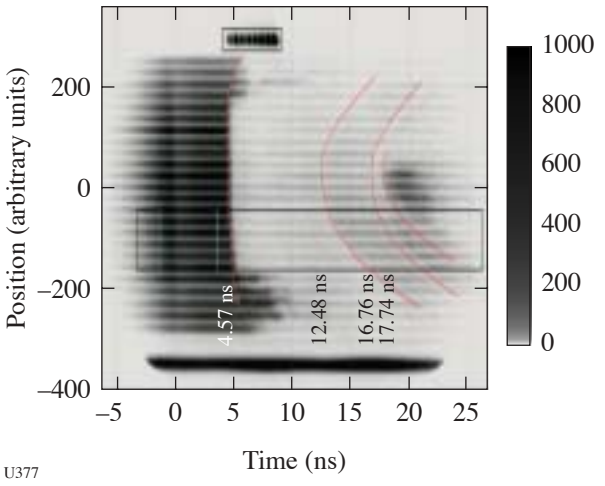


Figure 96.69
VISAR results of shot #30759: $H_2$ precompressed to 3.6 kbar.

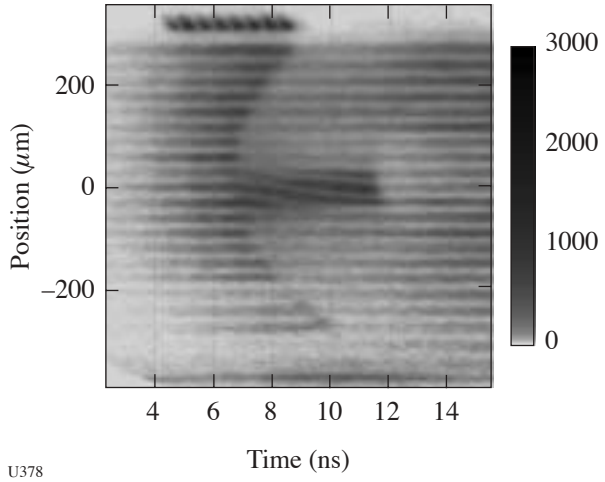


Figure 96.70
VISAR results from shot #31457: $N_2$ precompressed to 5.2 kbar.

After the shock leaves the sample, it travels through a 1.2-mm-thick single-crystal diamond cut in the (100) direction. Under weak shock loading, it is found that the diamond shears along four equivalent (111) planes, leaving a distinct fourfold symmetric fracture on the diamond table (Fig. 96.71). Considering the diamond's thickness, the shock assumes a somewhat spherical front so that the shock travels in different crystallographic directions within the diamond. It is reasonable to expect that the shock velocity, and hence the shock intensity, will reflect the symmetry of the diamond lattice. In fact, evidence of this symmetry breaking was observed by examining the recovered and deformed tungsten carbide support. When the tungsten carbide remained intact under strong shock loading, the deformation was not uniform, adopting a fourfold symmetry often characterized by a series of steps or "terraces" (Fig. 96.72). These terraced indentations occur where shear fractures along different (111) planes intersect, suggesting regions of greater stress in the diamond crystal (Fig. 96.73). It is noted that the fourfold symmetric strain cannot be caused by the tungsten carbide itself since it is amorphous and has no intrinsic fourfold symmetry.

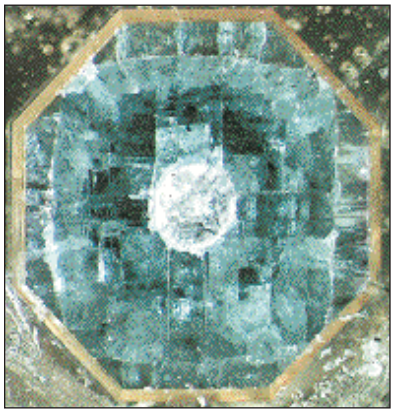


Figure 96.71
Photograph of diamond table showing central spall and four-fold shearing along (111) planes.

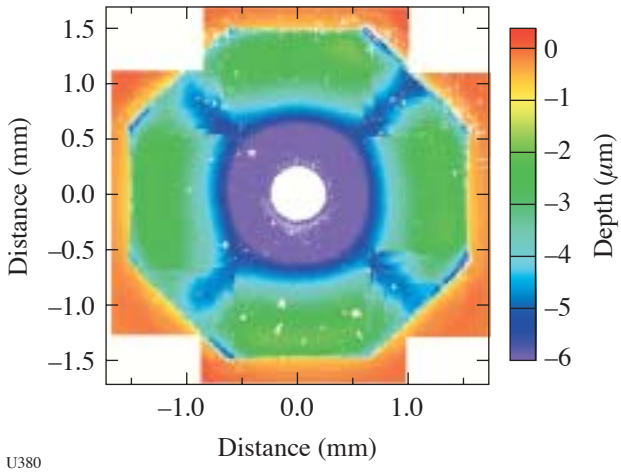


Figure 96.72
Depth profile of tungsten carbide support.

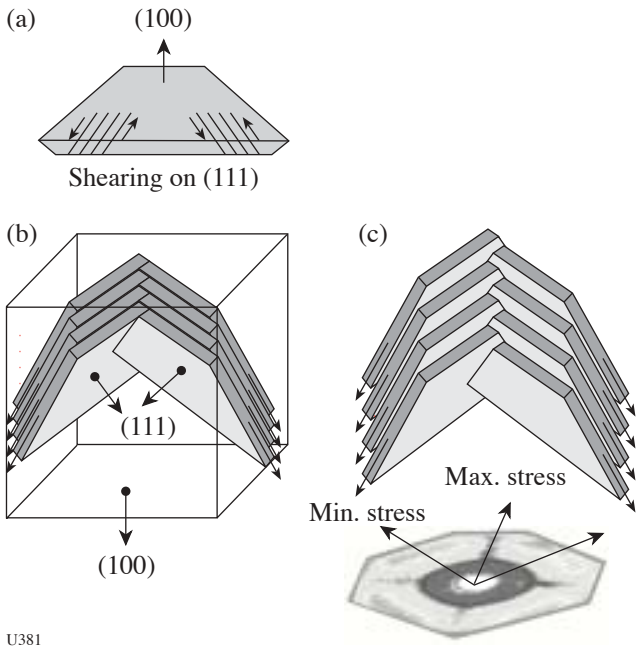


Figure 96.73
Illustration of shearing mechanism and relation to the plastic deformation in the tungsten-carbide backing plate.

During the second year of this study, the experiments will focus on determining the reflectivity transition and pressure–density equation-of-state measurements in hydrogen, helium, and nitrogen at several precompression pressures. New experimental approaches will also be developed to employ higher precompression pressures above 100 kbar so that regions of phase space can be accessed where exciting new predictions for the hydrogen phase diagram have been made, including a first-order dissociation in the liquid and a negative Clapeyron slope for the melt line at high pressures. Studies of the recovered material from the samples, to investigate expected phase changes such as the formation of graphite, amorphous carbon, and crystalline tungsten carbide, as well as searches for any new unpredicted phases, will continue.

## FY03 LLNL OMEGA EXPERIMENTAL PROGRAM*

In FY03 Lawrence Livermore National Laboratory (LLNL) continued to be a major user of OMEGA. LLNL's 390 experimental shots can be divided into two groups: those in support of the inertial confinement fusion (ICF) program and those in support of high-energy-density sciences (HEDS), which include materials, equation-of-state, and physics experiments.

### *ICF Experiments*

The ICF program on OMEGA in FY03 totaled 152 shots. Highlights of these experiments include the following:

*Charged-Particle Spectroscopy (CPS):* These implosions, done in collaboration with MIT, measured the charged fusion reactions produced from indirectly driven ICF implosions. Initial experiments ascertained the feasibility of using multiple CPS diagnostics as a measure of implosion asymmetry.

*X-Ray Thomson Scattering:* These shots showed that He- and H-like Ti x rays can be spectrally measured after scattering off near-solid-density plasmas. Theoretical fits to the data are in good agreement, opening the way for using this as a diagnostic for pusher $\rho R$ on National Ignition Facility (NIF) implosions.

*Cocktail (Mixtures of Materials) Hohlraums:* These experiments were performed to attempt to measure a predicted improvement in x-ray conversion efficiency and soft-x-ray albedo. Preliminary results seem to verify the latter, but not the former.

*Planar Rayleigh–Taylor:* A series of experiments were performed on polyimide targets to assess its usefulness as an ablator for ICF capsules. The data to date indicate a higher RT growth rate than calculated, even though acceleration measurements seem to match predictions.

*Technique Development:* A number of experimental techniques expected to be used on the NIF were tested with OMEGA shots. These included high-magnification x-ray imaging of imploded capsules, using target-mounted pinholes (Fig. 96.74), and development of a Kirkpatrick–Baez (KB) x-ray microscope with a spectrally narrow bandpass to look at x-ray line emission from a backlighter through a capsule. Additional experiments, done in collaboration with the University of Nevada–Reno, investigated spatially resolved spectroscopic measurements of pusher density using a Ti dopant within the inner layer of the capsule, while using Ar x-ray emission from the fuel region to deduce temperatures and densities in that region (Figs. 96.75 and 96.76).

*Acknowledgment: This work was performed under the auspices of the U.S. Department of Energy by University of California Lawrence Livermore National Laboratory under contract No. W-7405-Eng-48.

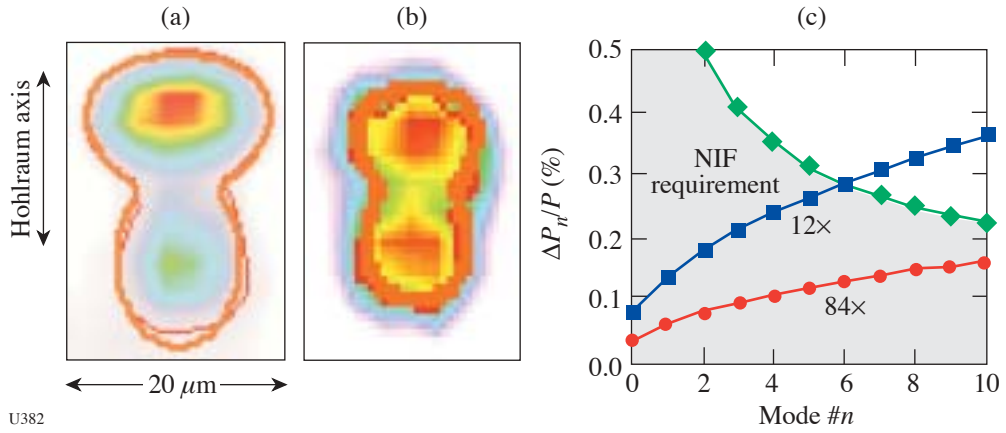


Figure 96.74
Examples of x-ray images taken with target-mounted pinholes of 5-$\mu$m aperture at a magnification of (a) 87× and (b) 12×. The resolution requirements of NIF targets are shown in (c) and compared to the achievable resolution of a 12× and 84× imaging system on the NIF.

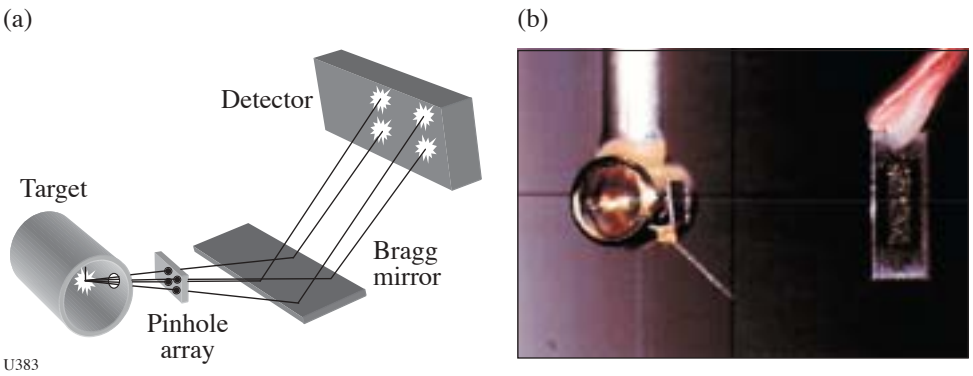


Figure 96.75
Illustration of a multi-monochromatic imaging (MMI) system based on an LLE-developed technique. Several MMI systems have been fielded for both LLNL and NLUF experiments on OMEGA: (a) schematic of MMI diagnostic illustrating the concept; (b) photograph of typical configuration used on hohlraum-driven experiments on OMEGA. Each device produces hundreds of 11-$\mu$m-resolution images. Spectral dispersion is achieved by a depth-graded $WB_4C$ multilayer mirror with an energy resolution of ~75. The devices typically cover the energy range of 3 to 5 keV.

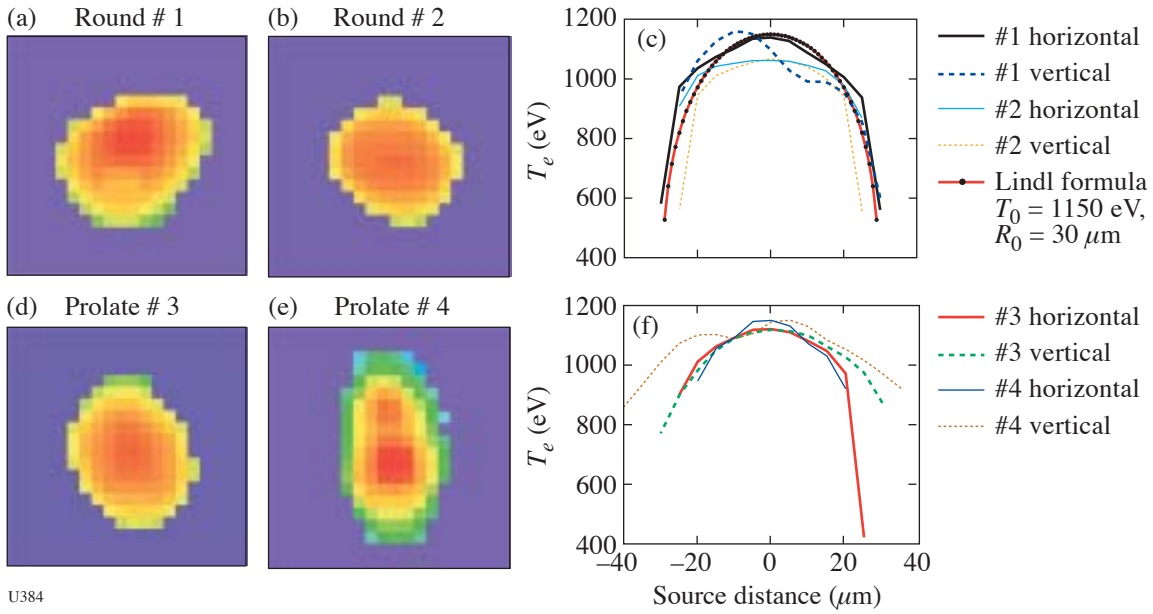


Figure 96.76
Inferred temperature maps taken on hohlraum-driven implosions of $D_2$-filled, Ar-doped capsules: (a), (b) 2-D temperature profiles, and (c) radial lineout of relatively round implosions; (d), (e) 2-D temperature profiles, and (f) radial lineout of prolate implosions.

*Laser–Plasma Interaction:* Laser–plasma interaction (LPI) experiments were carried out to explore the interaction of the laser with the large plasmas created when gas-filled hohlraums are used. Most of these experiments used gas bags as the initial target to provide a long-scalelength plasma with good diagnostic accessibility. Experiments measured Raman (SRS) and Brillouin (SBS) scattering levels, the effect of Langmuir damping, and energy exchange through SBS in crossed-beam experiments. The $4\omega$ probe beam was successfully used for Thomson-scattering measurements, as shown in Fig. 96.77. Additional experiments in gas-filled hohlraums investigated the effect of gas pressure on capsule hydrodynamics and possible enhanced gold–gas mixing due to preroughened hohlraum walls. Still another experiment searched for evidence of early-time laser light directly striking the capsule in indirect-drive experiments. These results are compared to calculations in Fig. 96.78.

Several high-yield, direct-drive DT implosions were carried out in collaboration with LANL to provide high fluxes of 14-MeV neutrons for diagnostic development. The characteristics of a photoconductive diamond (PCD) device in measuring neutrons is shown in Fig. 96.79. At high neutron flux, the impedance of the transmission line ($Z$) causes saturation at $I_{max} = V/Z$.

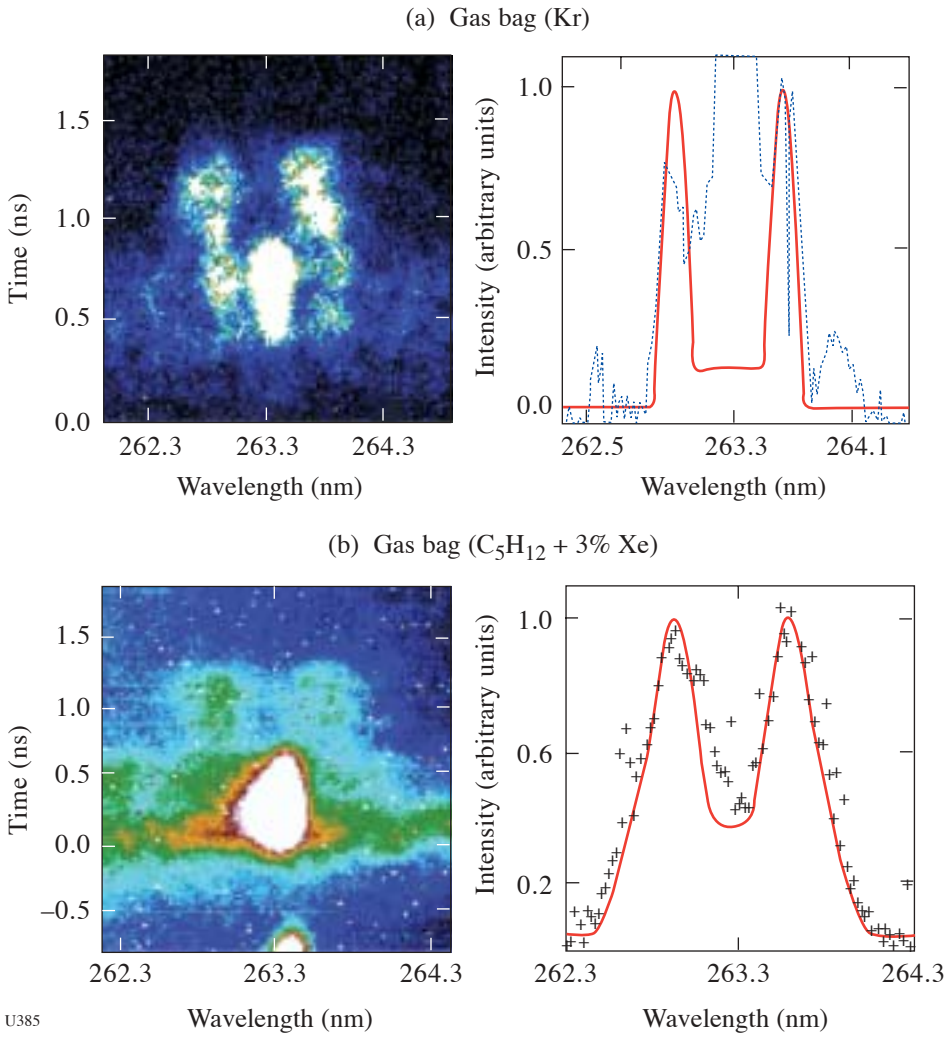


Figure 96.77
Illustrations of $4\omega$ Thomson-scattering measurements on laser–plasma interaction experiments: (a) streaked record of Thomson-scattering signal from a Kr-filled gas-bag target; (b) streaked record of Thomson-scattering signal from $C_5H_{12}$–3%Xe–filled gas bag. While the heater beams are on, these measurements show an electron temperature of ~3.2 keV for the Kr-filled gas bag. The $C_5H_{12}$–3%Xe–filled gas shows an electron temperature of 1.5 keV late in time.

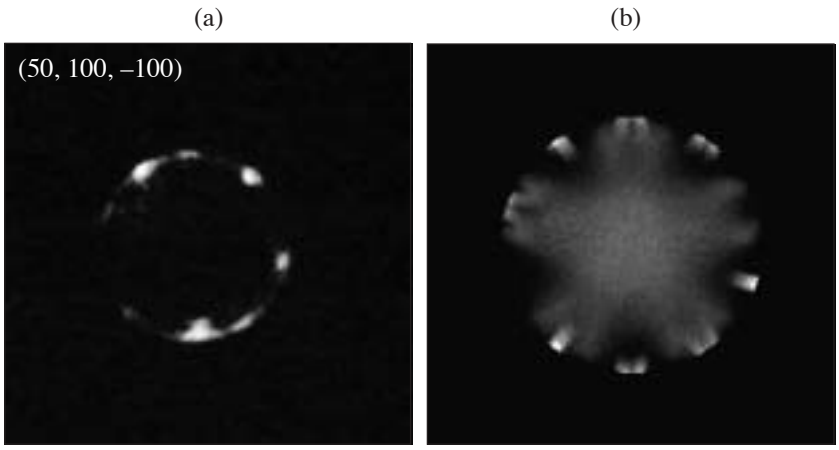


Figure 96.78
X-ray re-emission images are used to search for evidence of early-time laser light directly striking the capsules: (a) actual image; (b) experimental simulated image.

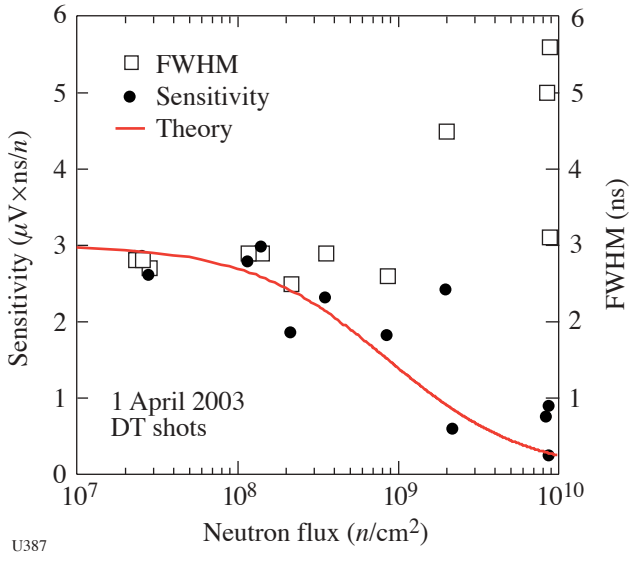


Figure 96.79
Experimental measurements of the sensitivity and full width at half maximum of the signal generated by a diamond detector in response to increasing neutron flux obtained from OMEGA experiments. The theoretical curve is from the x-ray work of Kania *et al.*[14]

### *HEDS/NWET Experiments*

The High-Energy-Density-Science and Nuclear Weapons Effects Testing (NWET) Programs used 238 laser shots on OMEGA during FY03. Some of the experiments included the following:

*IDrive:* A substantial number of shots ("IDrive") were devoted to developing techniques for measuring material properties when subjected to substantial pressures, but still in the solid state. Low-temperature Rayleigh–Taylor experiments were performed with this experimental arrangement (Fig. 96.80).

*NEL Preparation:* Another large group of shots were devoted to using OMEGA to prepare for NIF early-light (NEL) experiments. These included testing concepts for point-projection backlighting using backlit pinholes as an x-ray source. An example of this work in Fig. 96.81 shows an excellent radiographic image of a propagating shock.

*EOS Experiments:* Equation-of-state (EOS) experiments were performed in a variety of materials by measuring the velocity of ablatively driven shocks within the material. LLNL is a major participant in an NLUF experiment that measured shock velocities through precompressed gases within diamond anvil pressure cells, as shown in Fig. 96.82. Shock experiments were also used to measure opacities at elevated pressures and temperatures.

*Hot Hohlraums:* Experiments were conducted with small hohlraums to develop sources at elevated radiation temperatures.

*Convergent Rayleigh–Taylor:* Rayleigh–Taylor instabilities were studied in a spherically convergent geometry, using pre-imposed perturbations on spherical capsules.

*Double-Shell Capsules:* Double-shell (one shell containing DD fuel within another, concentric, indirectly driven shell) targets were explored for a number of properties, including their sensitivity to high-energy photon preheat, and the timing of the fuel shock heating compared to the timing of the fuel compression.

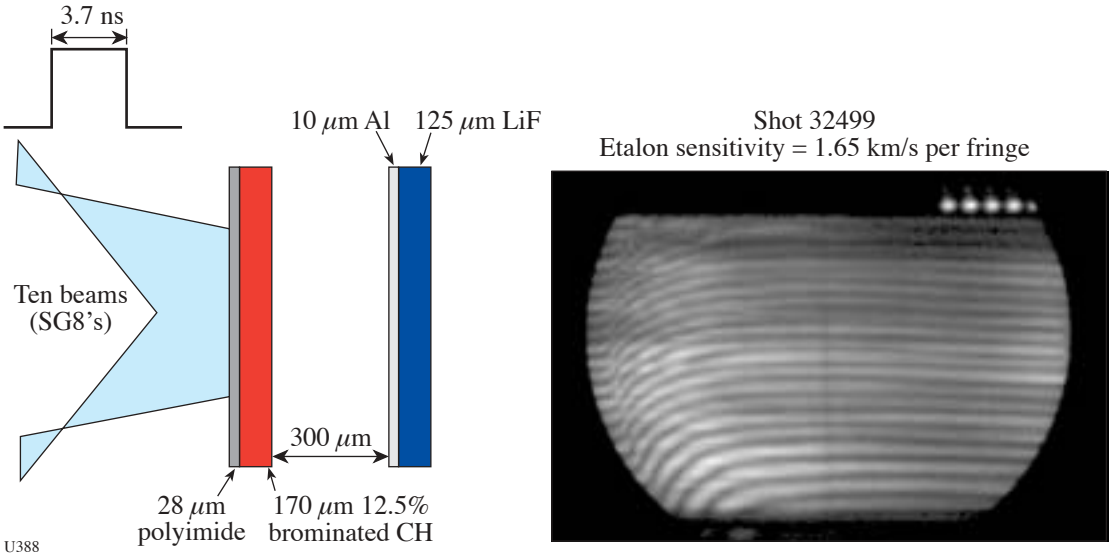


Figure 96.80
VISAR record on IDrive shot #32499 showing that smooth loading was achieved with no instabilities.

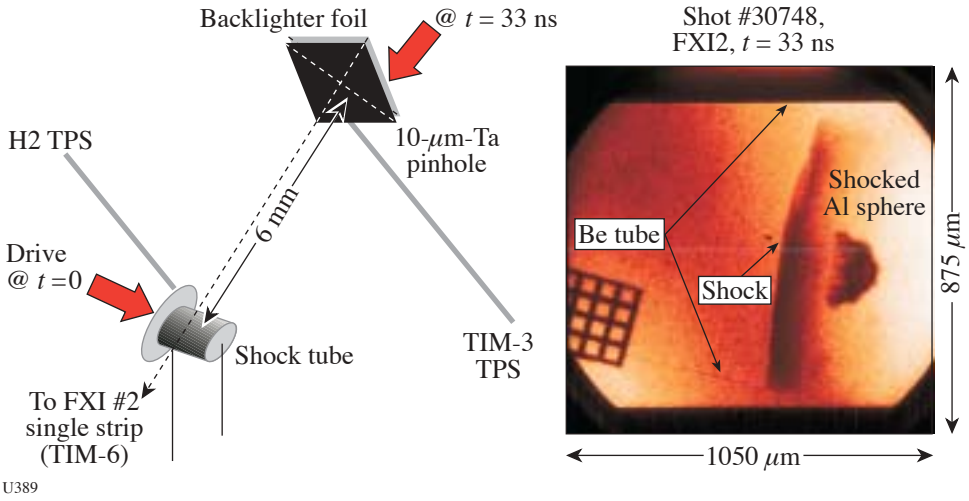


Figure 96.81
Illustration of the application of point backlighting to characterize the interaction of a shock with a spherical object.

*Radiation Propagation:* A number of experiments looked at the propagation of radiation in low-density materials.

*Dynamic Hohlraum:* Another experiment looked at the possibility of using a direct-drive configuration to create a dynamic hohlraum for driving implosions.

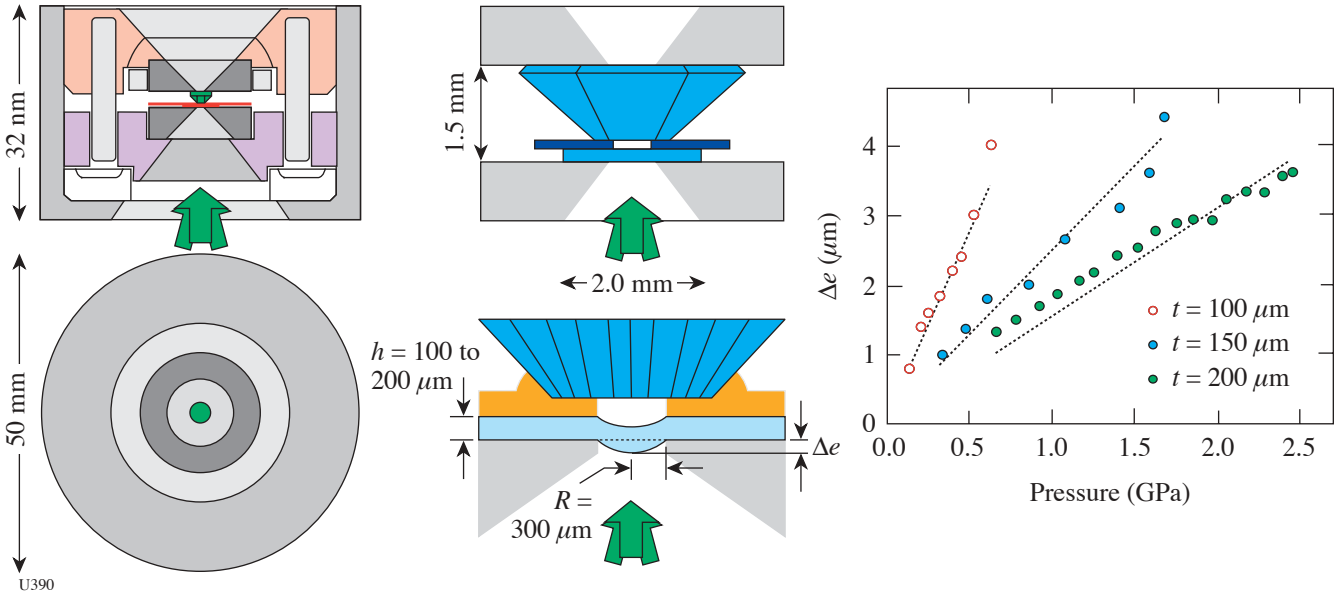


Figure 96.82
Experimental setup for an OMEGA equation-of-state experiment using a diamond anvil cell filled with a precompressed gas (such as hydrogen).

## FY03 LANL OMEGA EXPERIMENTAL PROGRAMS

The Los Alamos National Laboratory (LANL) series of experiments on OMEGA in FY03 emphasized research into hydrodynamic instabilities, mix, material properties, neutron diagnostic development, and radiographic technique development for the Nation's inertial confinement fusion and stockpile stewardship missions.

*Cylinder Implosions:* One phase of the hydrodynamic instability experiments investigates the Richtmyer–Meshkov instability (RMI) in a convergent, compressible, miscible plasma system in the presence of strong shocks.[15] Fifty of the 60 OMEGA lasers illuminate small, hollow, epoxy cylinders with 18 kJ of energy. The center cylinder is filled with low-density foam. A very thin aluminum marker layer is placed between the foam and the epoxy. The laser energy heats the epoxy cylinder to extreme temperatures, causing approximately one-half of it to vaporize and expand outward (away from the axis), while the other half is pushed inward (implodes) by a strong shock wave. The passage of the shock wave through the target assembly heats the target materials and causes them to become plasmas. As a result, the interfaces along both sides of the marker band are accelerated, and the materials mix over time. The danger of RMI is that in an ignition capsule, if the mixing becomes severe enough, fusion reactions end and thermonuclear ignition—the ultimate goal of all ICF experiments—fails. To measure the amount of mixing, five additional OMEGA laser beams strike an iron foil at one end of the cylinder after a small time delay. X rays are emitted, travel lengthwise through the cylinder, are imaged by a pinhole, and are recorded by a framing camera.

In a basic experiment conducted this year, a simple sinusoidal perturbation was machined into the outside of the aluminum marker layer, creating a corrugated surface with the corrugations running the length of the cylinder.[16] It was hypothesized that these perturbations would grow due to the convergence of the system and the shock-driven RMI. Furthermore, it was expected that the growth rate of the perturbations would change for different numbers of perturbations. Measurements were made with targets that had 8, 16, or 28 perturbations machined into them (Fig. 96.83). As can be seen in the

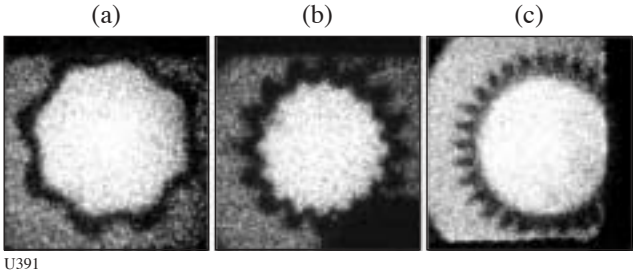


Figure 96.83
Axial radiographs of single-mode sinusoidally perturbed targets with mode numbers of (a) 8, (b) 16, and (c) 28. The dark band is the radiographically opaque aluminum marker layer.

figure, the amplitude of the corrugations at the outside of the marker layer is approximately the same in each case.

*Asymmetric Direct-Drive Spheres:* The asymmetric direct-drive spheres (ADDS) experiment tests the hypothesis that asymmetric implosions create more mixing of the shell material into the fusion fuel than do symmetric implosions. These directly driven 1100-$\mu$m-diam capsules were made of Si-GDP glass and filled with various pressures of DT. The convergence ratio was adjusted by varying the gas-fill pressure. The degree of asymmetry was varied from oblate to symmetric to prolate by adjusting the energy in each individual laser beam to make the correct overall pattern on the capsule.

This year, higher convergence implosions were conducted by reducing the fill pressure to 2.5 atm. These experiments had more mix than previously observed with 10 or 15 atm of gas fill. Figure 96.84 shows an x-ray image of a prolate implosion taken by the GMXI. Shell material can be seen all the way to the center. The yield was less affected by asymmetry in this experiment than it was with the 5 or 10 atm of gas fill.

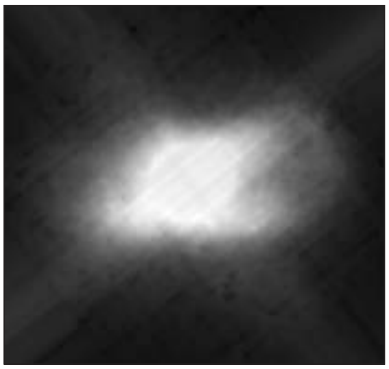
U392

Figure 96.84
A GMXI x-ray image of a prolate implosion showing that shell material has reached the core of the imploding capsule.

*Neutron Diagnostics Development:* In collaboration with Lawrence Livermore National Laboratory, symmetric implosions of DT-filled capsules aided the development of the carbon-vapor–deposited (CVD) diamond detector and the palm-top LANSA. These experiments also supported further development of the pinhole-based neutron imaging technique.

*Double-Shell Targets:* Direct-drive double-shell targets may provide an alternative, noncryogenic path to ignition on the National Ignition Facility (NIF).[17] Experiments are being pursued on OMEGA to understand the hydrodynamics of these implosions and the possibility of scaling them to NIF designs. The double-shell campaign examines the effect of drive, externally applied radiative preheat and foam composition on the implosion hydrodynamics, and the growth of mix due to hydrodynamic instabilities in a spherical geometry. Marker layers are implanted strategically in the capsule, and low-resolution radiography has been used to measure the zero-order hydrodynamic evolution of the capsule.

Twenty of the OMEGA laser beams were needed for backlighting, leaving only 40 beams to drive a symmetric implosion. The pointing of the remaining beams was offset from the center of the capsule to achieve a symmetric implosion. Radiographs were obtained from two different directions at multiple times with uniform area backlighting. A typical radiograph of a symmetric implosion is shown in Fig. 96.85. Neutron implosion data was also obtained simultaneously.

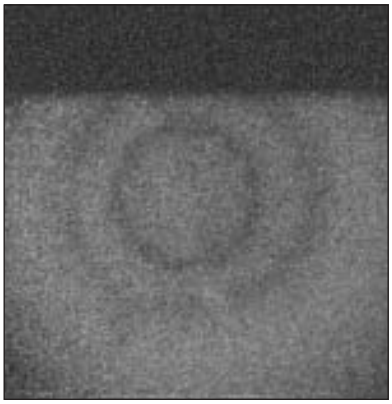
U393

Figure 96.85
A radiograph of a double-shell implosion target 1.7 ns after the beginning of the laser beams. The inner and outer shells and the intershell foam are clearly evident.

*Supersonic Jet:* In recent years we have fielded numerous supersonic-jet experiments[18] on OMEGA in a collaboration between Los Alamos National Laboratory, the Atomic Weapons Establishment, Lawrence Livermore National Laboratory, the University of Michigan, and the Laboratory for Laser Energetics. These experiments help validate our next-generation radiation-hydrodynamic codes. One of the outstanding questions is whether these types of jets should become turbulent, given their high Reynolds number. We have recently modified our experiments to have more Kelvin–Helmholtz shear, to run much later in time, and to increase the chance of going turbulent. To diagnose these large (several-millimeter) jets at very late times (100 to 1000 ns), we are developing

pinhole-apertured point-projection x-ray imaging (PAPBL) using an x-ray energy of about 5 keV.

This year's experiments have concentrated on validating a new target design and overcoming technical problems arising from the PAPBL imaging technique. High spatial resolution over a large field of view was demonstrated, and recent work has given unequivocal evidence of a jet in late-time radiographs. The experiment consists of a directly driven titanium "slug" that impacts a low-density foam. The jet of titanium formed in the carbonized-resorcinal-formaldehyde (CRF) foam is diagnosed by point-projection radiography.

Significant progress was made this year in utilizing pinhole-apertured x-ray point backlighting. Adequate backlighter intensity was obtained by using two laser beams (400 J per beam, 1-ns pulse length). Figure 96.86 shows a pinhole-aperture point-projection radiograph from the region of the resolution grid from a static-target experiment. Best fit to the experimental data is obtained by convolving a 15-$\mu$m FWHM Gaussian point-spread function with the ideal, theoretical grid transmission. This spatial resolution is comparable to that obtained in our previous pinhole-imaging experiments. The field of view of the earlier experiments was limited, however, to approximately 500 $\mu$m by the area-backlighting source, whereas that of the present point-backlit experiment covers approximately a 4-mm field of view. This represents a very significant potential increase of "information content" in comparison with the earlier work.

The new target design with PAPBL imaging successfully recorded clear evidence of the jet and the surrounding bow shock in the CRF foam (Fig. 96.87). Extensive design calculations for these experiments have been carried out at LANL

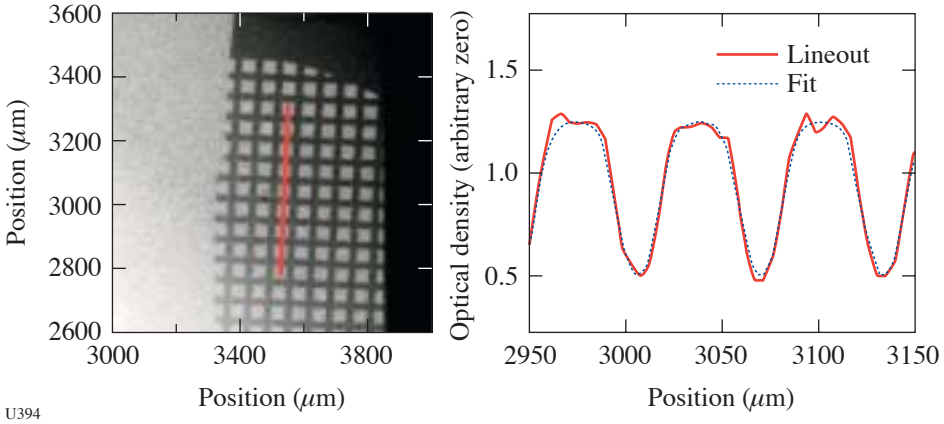


U394

Figure 96.86
Pinhole-aperture point-backlighter image of a static (not-driven) target. Best fit to the transmission of the image of the resolution grid is obtained when the ideal grid transmission is convolved with a 15-$\mu$m FWHM Gaussian spatial-resolution function.

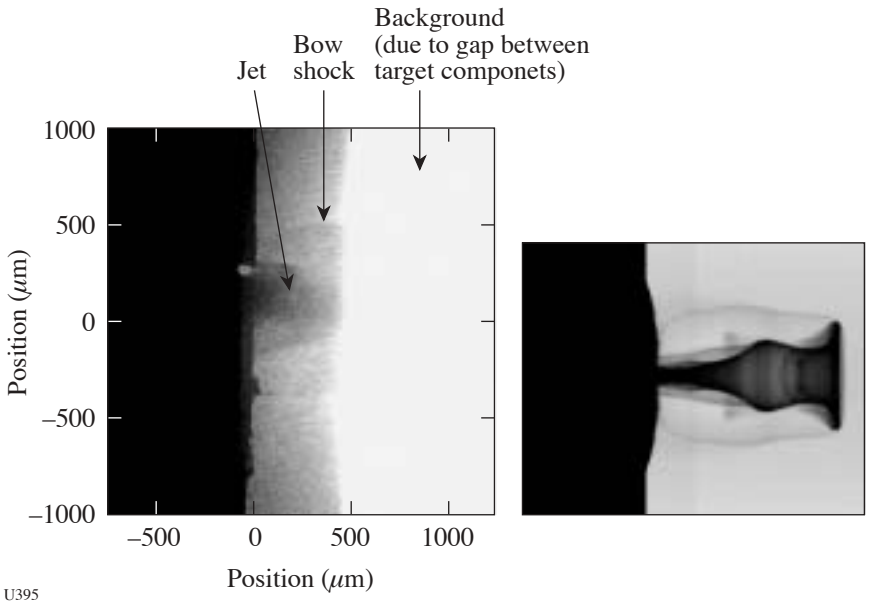


U395

Figure 96.87
Pinhole-aperture point-projection radiographic image of the titanium jet and bow shock in CRF foam and an NYM-PETRA simulation (shown at the same spatial scale). The experimental image is partially overlaid by background emission from the target, arising from an unintentional gap between target components.

using the *RAGE* code, and at AWE using the NYM and PETRA codes. Figure 96.87 also shows a simulated radiograph generated by NYM-PETRA. Careful analysis of the experimental images from our most-recent run indicates that the data in Fig. 96.87 are partially obscured by a region of emission resulting from an unintentional gap between the gold shield and titanium washer of the experimental package. A silver-loaded epoxy fillet, or modified shield design, would presumably reduce this problem in future experiments.

*Time-Dependent Mix:* The goal of the time-dependent mix experiment is the production of high-quality, time-resolved spectroscopic and imaging data that will constrain models of fuel–pusher mix in directly driven ICF implosions. The primary diagnostic marker is a thin (0.1-$\mu$m-thick) titanium-doped CH layer introduced at the fuel–pusher interface of an ICF capsule. The timing and intensity of emission from H-like Ti have been calculated to depend on the timing and amount of Ti that reaches the center of the fuel. In the first experiments, high-quality, time-resolved Ti *K*-shell spectroscopic data were obtained from targets that had a range of shell thicknesses and fill-gas pressures. The high quality of the data indicates the viability of this approach.

*X-Ray Backlighting:* Los Alamos also developed an x-ray-backlighting technique at 9 keV that produces uniform, large-area, monochromatic, high-resolution images of targets used for laser-driven AGEX and high-energy-density-physics (HEDP) experiments. X-ray imaging at moderate energy in laser-driven HEDP experiments is an essential, well-established tool for observing dynamic phenomena such as shock trajectories, interface motion, and instability growth. However, the standard technique using an area backlighter, coupled with the size of the object to be radiographed, requires an inordinate amount of laser energy to produce a monochromatic x-ray source above 7 keV.

High-resolution images were obtained using a pinhole-apertured point-backlighter (PAPBL) geometry and a Zn source. Figure 96.88(a) shows the raw image, recorded on x-ray film, of a thin-walled gold hohlraum used for radiation-driven experiments. Figure 96.88(b) shows the hohlraum in the center with 12 laser beams "driving" it. The top right corner shows the backlighter substrate while the object in the lower left-hand corner is the diagnostic camera. The high resolution, large dynamic range, and penetrating ability of the 9-keV x rays are apparent.

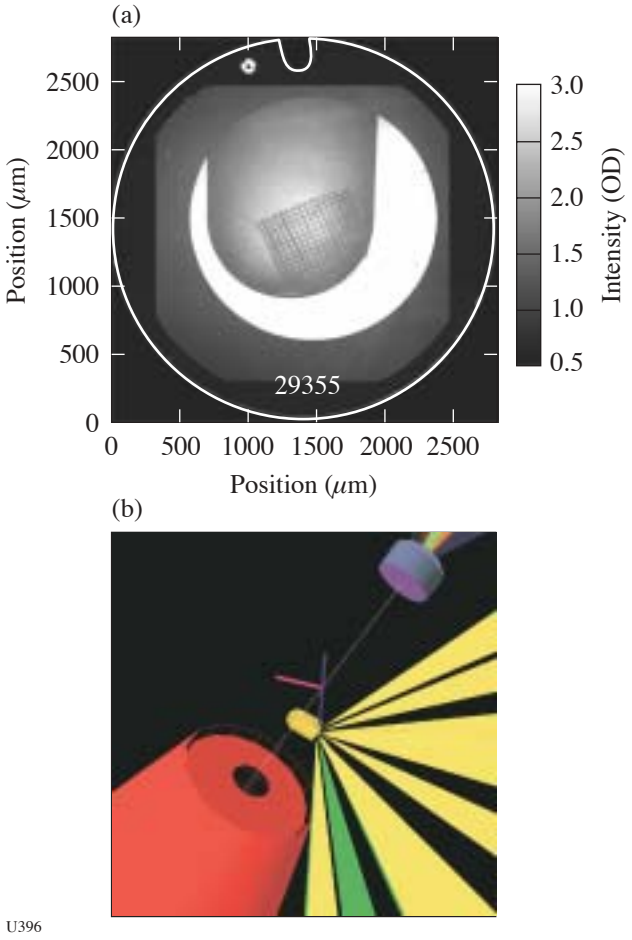


Figure 96.88
(a) Static x-ray radiograph with a 9-keV backlighter of a hohlraum with a resolution grid attached. A 62-$\mu$m (20-$\mu$m bar width) period grid was used for spatial calibration. (b) Configuration showing diagnostic nose tip, hohlraum, and backlighter substrate.

*Beryllium Ablative Microstructure Stability (BAMS):* Materials experiments concentrate on measuring the shock-propagation properties of beryllium because beryllium-based alloys are prime candidates for the NIF capsule material. Since the fusion yield depends strongly on the symmetry of the capsule during implosion, the importance of the elastic anisotropy of Be in the seeding of hydrodynamic instabilities is paramount. To measure this effect directly, Los Alamos began a series of beryllium ablative microstructure stability (BAMS) experiments. To that end, a 6-ns laser pulse was designed to achieve radiation pressure in a hohlraum environment to drive over 50 Rayleigh–Taylor growth times. LLE personnel have fabricated two separate pulse shapes, carried by 13 phased beams, which closely approximate the desired drive. Preliminary analysis of radiation temperature data (Dante and VISAR) indicates close agreement with calculations.

A small Be patch was mounted on the rear wall of the hohlraum opposite the laser entrance hole. Face-on x-ray radiography in the first experiment was used to assess the influx of Au from the hohlraum walls into the diagnostic line of sight and to observe machined perturbations in a Be-Cu (0.9% by atom) alloy. Self-backlighting by Au near the laser entrance hole shows growth of the 100-$\mu$m period perturbations with evidence of a Be bubble forming near the target axis (Fig. 96.89). Future experiments will optimize radiography techniques and possibly employ gas-filled hohlraums to inhibit Au transport toward the axis.

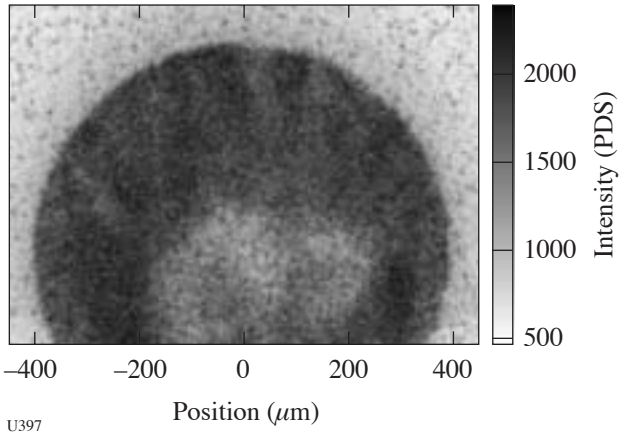


Figure 96.89
A radiograph of a sample Be backlit by Au emission within the hohlraum. The fringes correspond to the 100-$\mu$m period of machined perturbations in the Be patch. The light area on axis could be Au opacity or exclusion of Au by a Be bubble arising from the patch.

## FY03 SNL OMEGA PROGRAMS

Sandia National Laboratories (SNL) carried out a total of 30 target shots on the OMEGA laser in FY03 and also participated in several of the campaigns led by other laboratories. The SNL-led campaigns included the following:

*SOP/Aluminum Wedge Verification of Hohlraum Drive Temperature and Shock Temperature:* In FY03, streaked optical pyrometer (SOP)[19] measurements of the shock velocity in aluminum wedges were begun on OMEGA to verify hohlraum radiation temperature. The aluminum wedges in these experiments were fielded side by side with indirect-drive ICF ablator samples for the purpose of SOP intensity calibration at the 280±20-nm bandpass. As was done years ago on Nova, this data can also be used, however, to verify the hohlraum radiation temperature.[20,21] There were some surprises in this new data. Figure 96.90(a) shows a comparison of the pre-shot calculation with the unfolded Al-wedge SOP data from OMEGA shot 31819 (5.56 kJ, 2 ns square). The measured Al shock velocity was about 12% higher than predicted in the pre-shot *LASNEX* calculations. The result of a post-shot calculation using a drive multiplier to match the data is also indicated in the figure. Figure 96.90(b) shows the overlay of a DANTE[22] measurement for a very similar previous hohlraum experiment done on a P6-P7 axis (OMEGA shot 27564; 5.53 kJ, 2 ns). It appears that both the post-shot and pre-shot versions of the drive are close to bounding the uncertainty of the DANTE measurement; however, the same conclusion is not reached in our analysis of the similar experiment employing a 1-ns drive. In this experiment (OMEGA shot 31820), the measured Al velocity was about 25% higher than the pre-shot prediction.

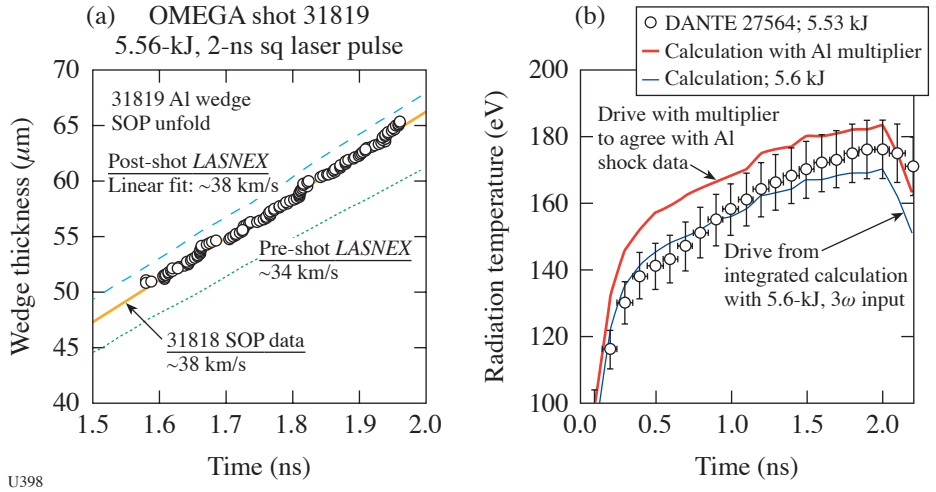


Figure 96.90
(a) Unfold of shock position versus time for Al wedge in OMEGA shot 31819 (5.56 kJ, 2 ns square) compared to pre-shot and post-shot *LASNEX* calculations. (b) Comparison of Dante unfold from OMEGA shot 27564 (5.53 kJ, 2 ns square) with drive from shot 31819 pre-shot and post-shot calculations.

These hohlraum drive measurement comparison issues will be explored further in the FY04 SNL campaign.

*Experimental Verification of Shock Temperature and Preheat Reduction in Doped Ablator Samples:* In FY03, the streaked optical pyrometer (SOP)[19] was used to view the preheat and shock breakout in side-by-side samples of doped and undoped indirect-drive ICF ablator samples. A key result was the experimental demonstration of preheat and shock temperature reduction via the use of mid-*Z* dopants in the low-*Z* ablator material.[23,24] Figure 96.91(a) shows the SOP image from OMEGA shot 31821 in which side-by-side, wedge-shaped samples of $C_{38}H_{60}O_2$ and $C_{39}H_{57}O_2Ge_2$ were driven by a hohlraum radiation pulse. It is clear from the image that the intensity levels of the preheat and the shock breakout are significantly reduced in the Ge-doped sample. Figures 96.91(b) and 96.91(c) show overlays of the intensity–time lineouts of side-by-side doped and undoped samples driven at hohlraum temperatures of ~160 eV (OMEGA shot 31818, 2 ns square) and ~200 eV (OMEGA shot 31821, 1 ns square). It found that the ~8× reduction in preheat and the 2× reduction in shock temperature are approximately consistent with *LASNEX* calculations that employ opacities based on the techniques of Refs. 25 and 26. Similar side-by-side experiments using undoped and Cu-doped beryllium samples are planned for early FY04. A new issue arising with this data is illustrated in Fig. 96.92. As indicated in the figure, the detailed analysis of the Ge-doped CH-wedge measurements indicates a shock velocity that is ~12% to 15% lower than the *LASNEX* calculations. This result would appear to be in contradiction to the Al-wedge results (see previous section) in which Al shock velocity is found to be higher than the *LASNEX* prediction (a result that is found even in the experiment employing side-by-side wedges of Al and Ge-doped CH). This issue will also be explored further in FY04.

*Indirect-Drive ICF Ablator X-Ray Burnthrough Measurements:* To achieve indirect-drive ignition of an ICF capsule, ablator burnthrough timing must be predicted to within a few percent. In FY03, the techniques described in Ref. 27 were employed to begin using the streaked x-ray imager (SXI) diagnostic[28] to view time-resolved x-ray burnthrough in side-by-side samples of ablator materials having different thicknesses or dopant levels. An example of this new data is shown in Fig. 96.93. The fact that the signals from the doped and undoped CH do not overlay with 700-eV offset is consistent with the calculations only if a significant contribution of second-order, 1.4-keV flux is included. This represents a new unresolved issue: the result is contrary to our past experience with the SXI data. Another interesting new issue that has come up in the SXI data that is related to the discussions of the two previous sections is illustrated in Fig. 96.94. Here, the new information on hohlraum drive is applied to the analysis of previous polyimide x-ray burnthrough data obtained in FY02. As indicated in the figure, it appears that the application of the new Al-wedge drive data leads to a significantly improved agreement between the calculated and measured x-ray burnthrough behavior.

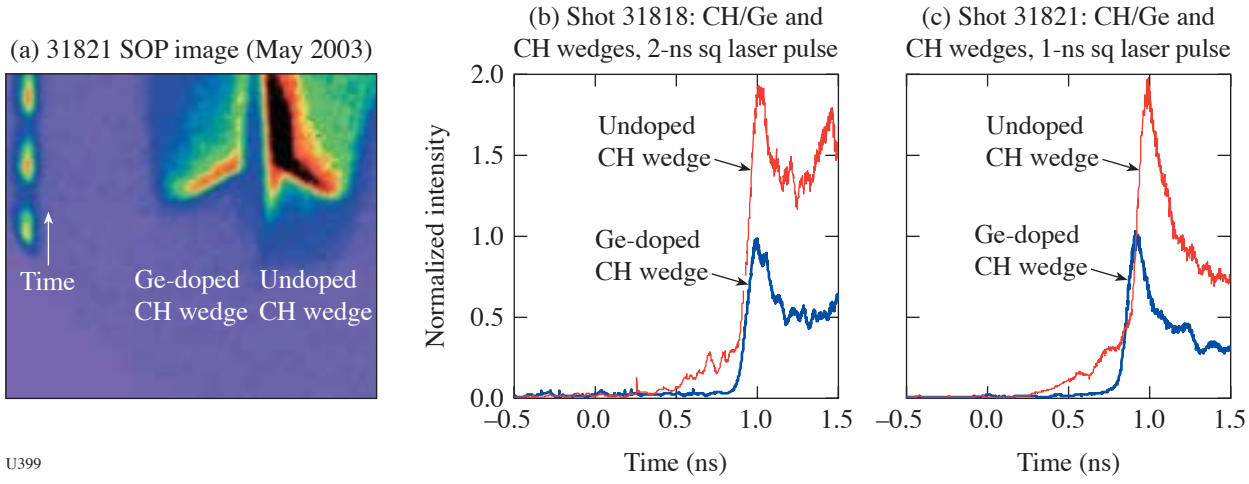


Figure 96.91
(a) SOP image from OMEGA shot 31821 in which side-by-side wedge-shaped samples of $C_{38}H_{60}O_2$ and $C_{39}H_{57}O_2Ge_2$ were driven by a hohlraum radiation pulse. (b) and (c) Overlays of the intensity–time lineouts of side-by-side doped and undoped samples driven at hohlraum temperatures of ~160 eV (OMEGA shot 31818, 2 ns square) and ~200 eV (OMEGA shot 31821, 1 ns square).

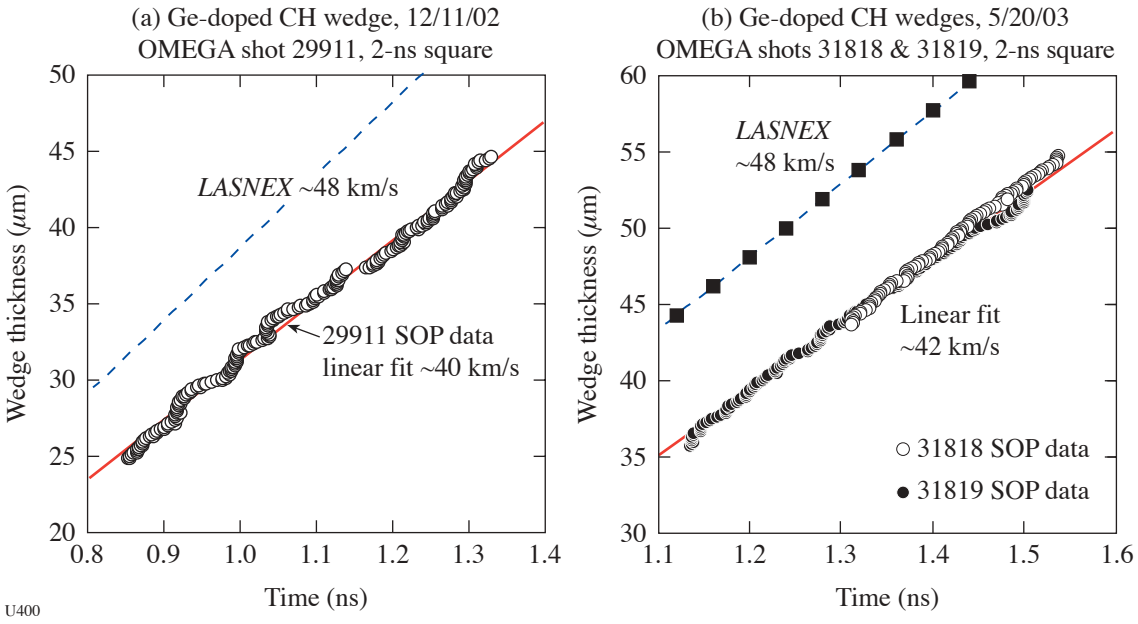


Figure 96.92
Unfold of shock position versus time for Ge-doped CH wedges in (a) OMEGA shot 29911 and (b) shots 31818 and 31819.

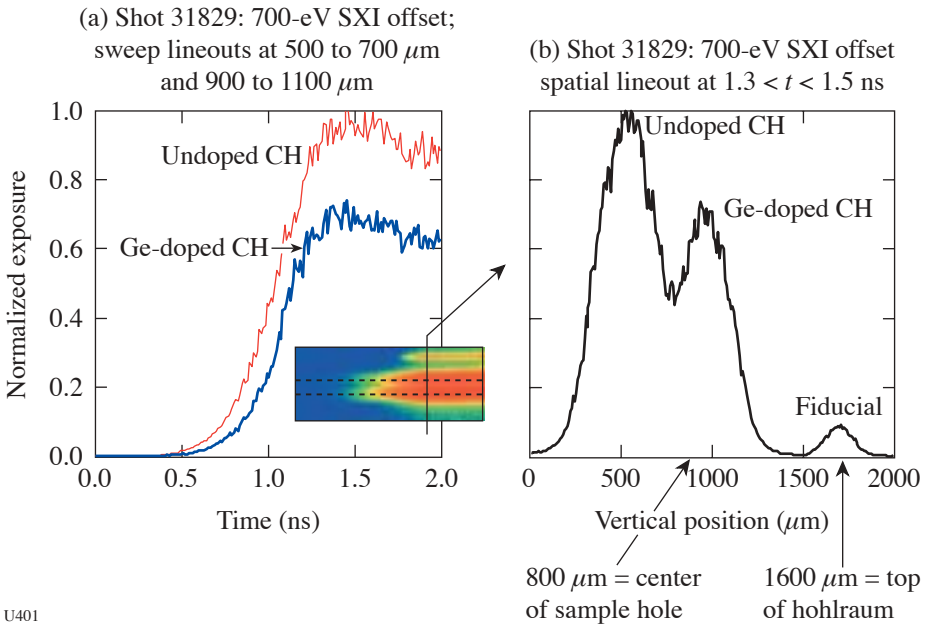


Figure 96.93
Spatial lineout through SXI streaked image including times between 1.3 and 1.5 ns for OMEGA shot 31829 employing side-by-side samples of Ge-doped and undoped CH.

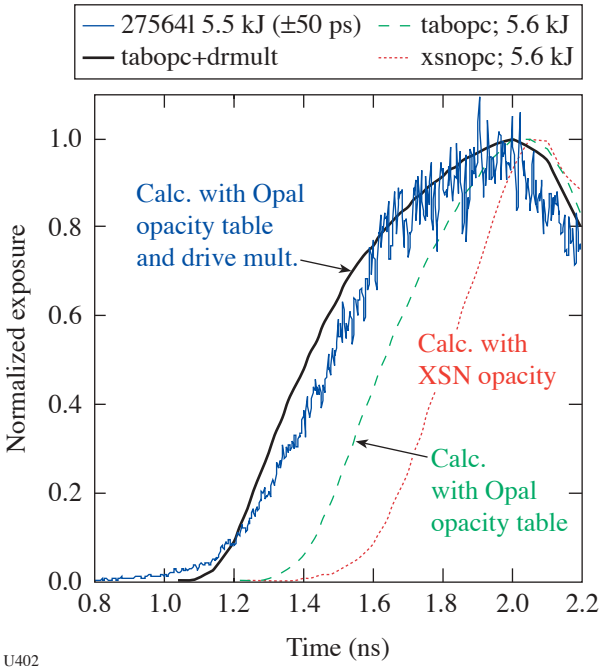


Figure 96.94
Comparison of *LASNEX* calculation variations to the SXI data lineout for OMEGA shot 27564.

## CEA PROGRAMS

The Commissariat à l'Énergie Atomique (CEA) of France was allotted three shot days on OMEGA in FY03 and carried out 32 target experiments. The experiments were focused in two primary areas: (a) laser–matter interaction and (b) diagnostics development.

### *First Tests of the DEMIN Spectrometer on OMEGA*

*a. Laser–Matter Interaction:* A new Thomson-scattering configuration for probing electron-plasma waves stimulated by Raman backscattering instability (SRS) was defined and successfully tested on OMEGA in FY03. In this experiment, two OMEGA beams at $3\omega$ were used to stimulate and probe electron-plasma waves in a plasma preformed by 40 heater beams. This configuration will be used to investigate the growth and saturation of SRS in gas-bag targets (Fig. 96.95) representative of the homogeneous plasmas that will be produced on the NIF and LMJ. For this study, Thomson scattering is a valuable complementary diagnostic of backscattering stations because it provides measurements that are spatially resolved along the interaction-beam propagation axis, thus demonstrating that SRS activity is occurring in a plasma representative of the NIF and LMJ.

*b. Diagnostics Development:* The DEMIN (detector micromegas for neutrons) neutron spectrometer[29] designed by CEA was tested for the first time during ICF experiments on OMEGA in FY03. The DEMIN concept, derived from the one used on high-energy physics,[30] is based on the association of a neutron-to-proton converter with a thin gas chamber (600 $\mu$m). This design has an efficiency of $10^{-3}$ and $10^{-6}$, respectively, for 14-MeV neutrons and 1-MeV photons. This intrinsic $\gamma$-ray insensitivity allows the measurement of secondary (DD target) and tertiary (DT target) neutrons in large $\gamma$ background. This $\gamma$ background is induced by $(n, \gamma)$ interaction on hardware present in the experimental area [noted $(n, \gamma)$ on Fig. 96.96].

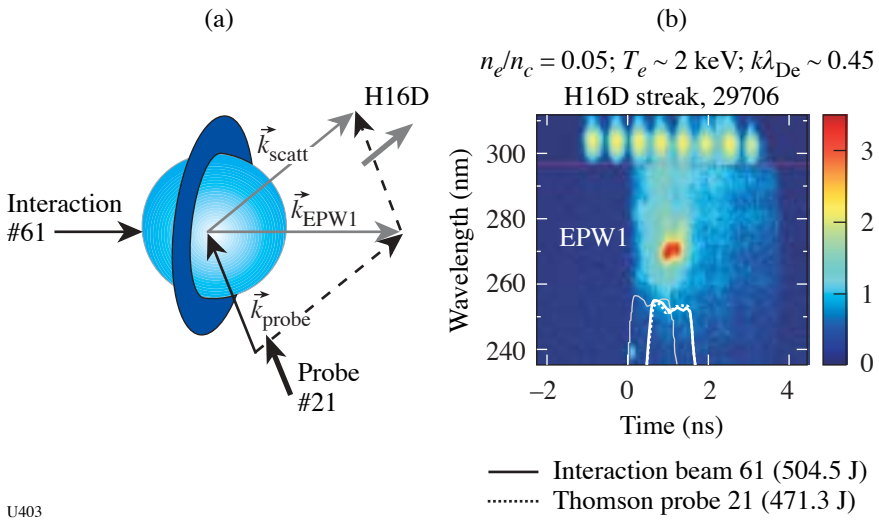


Figure 96.95
(a) Schematic of SRS experiment showing gas-bag target geometry with an interaction beam (61) and probe beam (21). (b) Streak camera recording of Thomson signal generated by scattering from electron-plasma waves generated by the SRS instability.

Recorded DEMIN signals show this relative $\gamma$ transparency by comparison with a calibrated scintillator plus photomultiplier tube (HCB12). Figures 96.96 and 96.97 present photon and neutron flux as a function of the time after the target implosion.

In both cases, the comparison of signals from DEMIN and HCB12 shows the intrinsic $\gamma$-ray insensitivity of the DEMIN spectrometer. Gamma rays induce small or non-observed signals in the time-of-flight window, where secondary and tertiary neutrons will induce signals with several tens of millivolts.

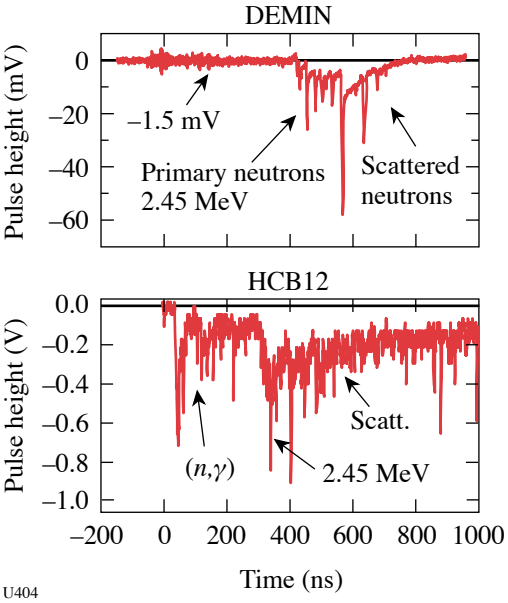


Figure 96.96
DEMIN record from DD target shot #31774. In the case of DD targets, $\gamma$rays do not induce signals before primary and scattered neutrons in DEMIN. The noise in the measurement time window of expected secondary neutrons (12 to 17 meV) is low (±1.5 mV). In this DEMIN configuration, secondary neutrons will give several tens of millivolts. By comparison, $\gamma$rays are clearly observed by the HCB12 detector and will mask any secondary neutron signal.

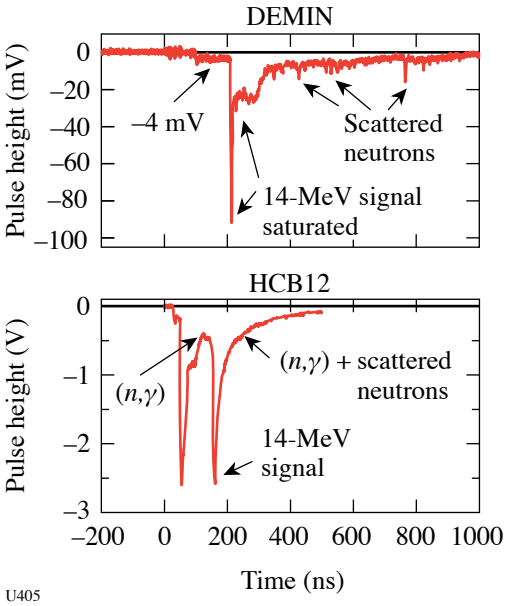


Figure 96.97
DEMIN record from DT target shot #31750. In the case of a DT target, the signal induced by the 14-MeV neutrons is saturated in DEMIN; the high yield of primary neutrons inhibits the electric field in the gas during few tens of nanoseconds. Whereas with the HCB12 detector the $\gamma$ rays signal is as important as for 14-MeV neutrons, the DEMIN exhibits a low signal (≤4 mV).

### *Fast Photoconductor for Neutron Spectroscopy: the SCANED Concept*

The SCANED (SCAttered NEutron Diagnostic) detector, designed by CEA, was tested during the DT shots campaign in May 2003. The concept is based on a photoconductor operating as a time-of-flight detector. The fast response of photoconductors is the main advantage, allowing location near the target; therefore, the neutron spectrum is recorded before the arrival of scattered neutrons and gamma rays produced on the chamber hardware. This concept is proposed for various measurements in ICF experiments: ion temperature, neutron yields, $\langle \rho R \rangle$ by secondary neutrons (DD target), and downscattered neutrons (DT target).[31,32] Moreover, photoconductors can be an alternative for diagnostics that may be inoperative with high yields (on the NIF and LMJ).

SCANED is composed of a *n*-irradiated AsGa detector ($6 \times 4$ mm$^2$) fixed in a 50-Ω loaded design made of plastic and Teflon to minimize $(n,n')$ and $(n,\gamma)$ interactions. Signals are recorded by a set of three IN7100 oscilloscopes to get a large dynamic range.

The goals of the experiments performed in May were the measurement of the sensitivity to 14-MeV neutrons and the study of noise, EM effects, and the duration of the tail in the pulse shape after the prompt 14-MeV neutron interaction.

Two SCANED setups were tested at 1 m and 0.385 m from target chamber center (TCC), respectively. Figure 96.98 shows a typical spectrum for the closest location. We easily observe 14-MeV and 2.45-MeV neutron peaks, from D+T and D+D fusion, respectively. The gamma background induced by the neutron interaction in the chamber skin is measured about 29 ns after the 14-MeV neutron signal. A DMX diode located between SCANED and the target (at 13.5 cm from the target) induces background over 10 ns after the x-ray signal is emitted by the target.

Work is in progress to improve the response of photoconductors.

### *Capillaries Detector for ICF Capsule Neutron Images*

14-MeV imaging detector arrays have been developed by assembling glass capillaries of 85-$\mu$m mean diameter into 100 $\times$ 100-mm$^2$ coherent arrays. The capillaries are filled with a liquid scintillator whose optical index is higher than the glass index. Neutron scattering of the hydrogen nuclei of the scintillator and the recoil ions produce light in several adjacent capillaries as they lose energy. The light distribution about the scattering point determines the detector spatial resolution. A 650-$\mu$m spatial resolution has been achieved; the resolution is enhanced to 325 $\mu$m by loading deuterium in the scintillator as the recoil deuterons have shorter mean free paths than recoil protons (Fig. 96.99). This array has been tested on the OMEGA neutron imaging system (NIS). These results will permit the achievement of high resolution in neutron images with moderate magnification ratio and practical line of sight on LMJ and the NIF.

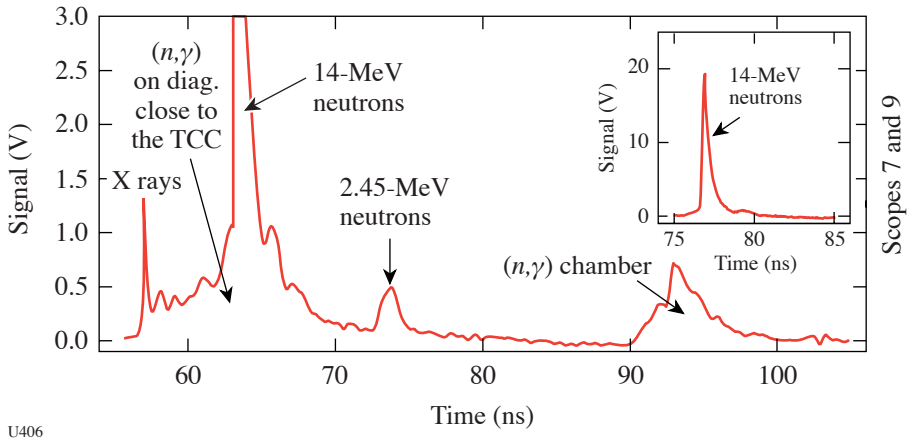


Figure 96.98
SCANED signal on shot 31756 (DT-filled target).

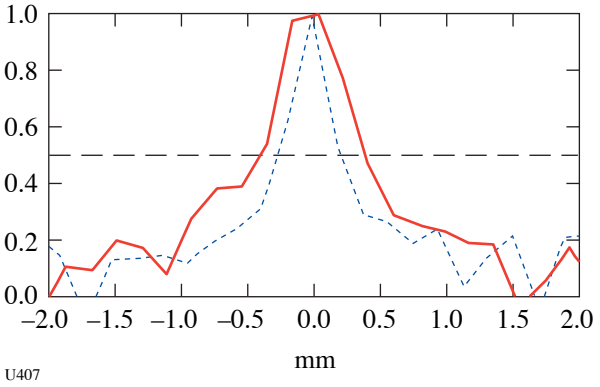


Figure 96.99
14-MeV neutron point-spread function measured in the 85-$\mu$m-diam capillaries array filled with a high-optical-index scintillator nondeuterated (solid line) and deuterated (dashed lines). Corrected from the 380-$\mu$m readout system resolution, the FWHM is 650 $\mu$m and 325 $\mu$m for the nondeuterated and deuterated scintillator, respectively.

### *Neutron-Induced Current Generation*

High-pulsed neutron irradiation can drive a transient current generation on coaxial cables. For intense, 14-MeV neutron irradiation that will exit on future ICF facilities such as LMJ in France and the NIF in the U.S., this effect can generate a signal on a 50-Ω load as high as a few hundred volts. On such a facility, coaxial cable will be widely used to transfer the electrical signals generated by the detectors placed close to the source to their recording devices placed away from the target to be sufficiently protected against the nuclear environment induced by this neutron irradiation. All of these cables will be affected by the parasitic signals induced by the pulsed neutron irradiation during high-yield neutron shots. No simple protective method (other than cumbersome 1-m-thick shielding) can protect the cable from this intense neutron irradiation. To investigate the potential level of this effect, OMEGA was used as an intense, pulsed, 14-Mev neutron source on direct-drive-yield neutron shots (up to $10^{14}$ neutrons of 14 MeV). OMEGA shots can induce a weaker but sufficient signal to be recorded if a coaxial cable can be placed sufficiently close to the target. In this case, a standard high-bandwidth coaxial cable (1/4-in.-diam, semi-rigid SMA type) was set at 25 cm on the neutron source by means of a diagnostic inserter (TIM). A weak but clear signal was recorded (Fig. 96.100).

Each weak bump on this recorded signal is associated with the 14-MeV neutron burst (time duration of 100 ps, which corresponds to a space extension of 5 mm) on each U-turn of the zigzag coaxial cable placed closest to the neutron source (see Fig. 96.101). In order to accurately time-reference each induced signals with respect to the time of neutron production, a standard x-ray diode was added at the end of the coaxial cable to record the instant of the neutron production (associated with a hard-x-ray burst). This time is represented by the signal bump #4, which corresponds to the arrival of the x ray on the diode. Each of the bumps is clearly identified due to the arrival of the neutron burst at each of the U-turns (bumps 1 to 6). Moreover, each signal generated by the neutrons on each U-turn is also reflected by the coaxial end and represents later bumps (7 to 11), so a clear time reference is associated with each bump and clearly shows the effect of pulsed neutron generation on a coaxial cable.

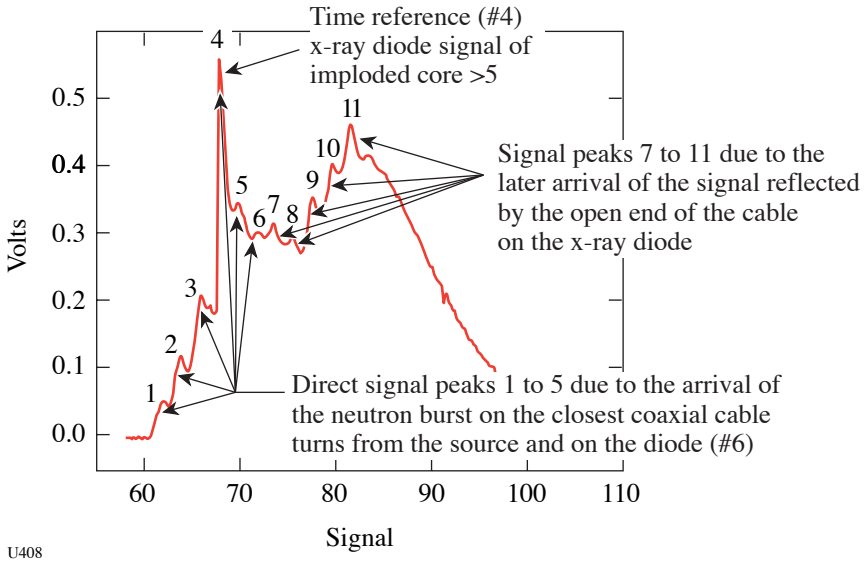


Figure 96.100
Signal recorded by a high-bandwidth (7-GHz), single-shot oscilloscope on high-yield OMEGA neutron shots.

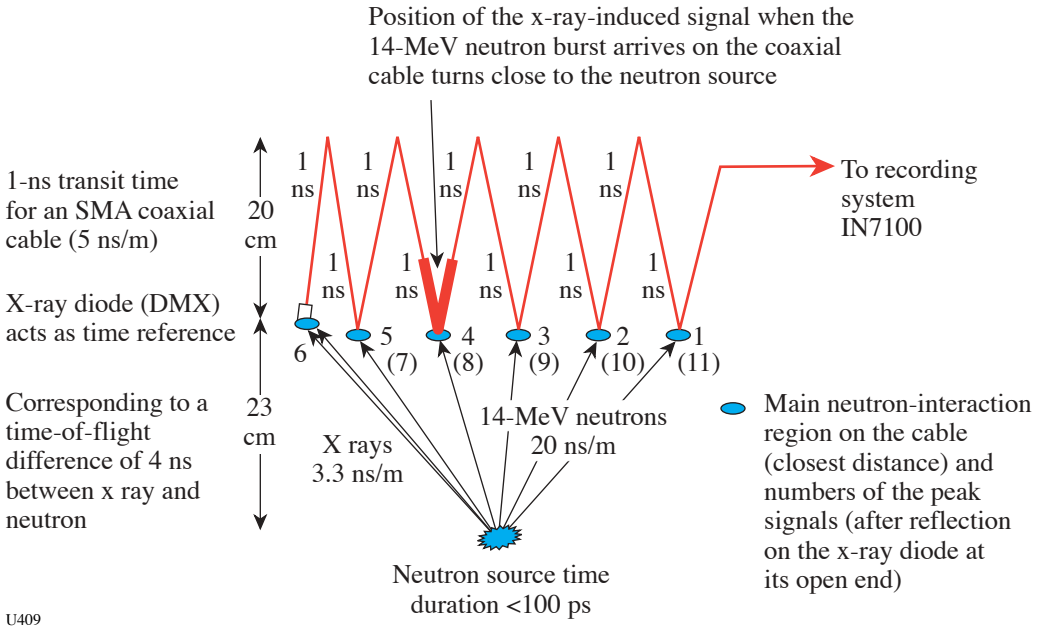


Figure 96.101
Schematic drawing of the experimental setup showing the origin of each signal bump.

## REFERENCES


1. H. F. Robey *et al.*, Phys. Plasmas **10**, 614 (2003).
2. P. A. Keiter, R. P. Drake, T. S. Perry, H. F. Robey, B. A. Remington, C. A. Iglesias, R. J. Wallace, and J. Knauer, Phys. Rev. Lett. **89**, 165003 (2002).
3. A. C. Calder *et al.*, Astrophys. J. Suppl. Ser. **143**, 201 (2002).
4. A. Miles, D. Braun, J. Edwards, H. F. Robey, R. P. Drake, D. R. Leibrandt, E. C. Harding, J. P. Knauer, and D. Arnett, "Numerical Simulation of Supernova-Relevant Laser-Driven Hydrodynamics Experiments on OMEGA," submitted to Physics of Plasmas.
5. R. P. Drake, B. A. Remington, and D. D. Ryutov, "Experimental Astrophysics with Intense Lasers," submitted to Review of Modern Physics.
6. R. D. Petrasso, J. A. Frenje, F. H. Séguin, C. K. Li, B. E. Schwartz, C. Stoeckl, P. B. Radha, J. A. Delettrez, D. D. Meyerhofer, S. Roberts, T. C. Sangster, and J. M. Soures, Bull. Am. Phys. Soc. **47**, 145 (2002).
7. B. E. Schwartz, F. H. Séguin, J. A. Frenje, R. D. Petrasso, C. K. Li, P. B. Radha, D. D. Meyerhofer, S. Roberts, T. C. Sangster, J. M. Soures, and C. Culligan, Bull. Am. Phys. Soc. **47**, 219 (2002).
8. C. K. Li, F. H. Séguin, J. A. Frenje, R. D. Petrasso, J. A. Delettrez, R. L. Keck, J. M. Soures, P. W. McKenty, F. J. Marshall, V. N. Goncharov, J. P. Knauer, D. D. Meyerhofer, P. B. Radha, S. P. Regan, T. C. Sangster, and W. Seka, "$\rho R$ Asymmetry in the Spherical Implosion of Inertial Confinement Fusion," submitted to Physical Review Letters.
9. R. I. Klein *et al.*, Astrophys. J. **583**, 245 (2003).
10. H. F. Robey, T. S. Perry, R. I. Klein, J. O. Kane, J. A. Greenough, and T. R. Boehly, Phys. Rev. Lett. **89**, 085001 (2002).
11. C. Stoeckl, R. E. Bahr, B. Yaakobi, W. Seka, S. P. Regan, R. S. Craxton, J. A. Delettrez, R. W. Short, J. Myatt, A. V. Maximov, and H. Baldis, Phys. Rev. Lett. **90**, 235002 (2003).
12. L. A. Welser, R. C. Mancini, J. A. Koch, S. Dalhed, R. W. Lee, I. E. Golovkin, F. Marshall, J. Delettrez, and L. Klein, Rev. Sci. Instrum. **74**, 1951 (2003).
13. L. A. Welser, R. C. Mancini, J. A. Koch, N. Izumi, H. Dalhed, H. Scott, T. W. Barbee, Jr., R. W. Lee, I. E. Golovkin, F. Marshall, J. Delettrez, and L. Klein, J. Quant. Spectrosc. Radiat. Transf. **81**, 487 (2003).
14. D. R. Kania *et al.*, J. Appl. Phys. **68**, 124 (1990).
15. N. E. Lanier *et al.*, Phys. Plasmas **10**, 1816 (2003).
16. M. M. Balkey *et al.*, "Production and Metrology of Cylindrical Inertial Confinement Fusion Targets with Sinusoidal Perturbations," Los Alamos National Laboratory report LA-UR-03-3682 (2003); to be published in *Fusion Science and Technology*.
17. W. S. Varnum, N. D. Delamater, S. C. Evans, P. L. Gobby, J. E. Moore, J. M. Wallace, R. G. Watt, J. D. Colvin, R. Turner, V. Glebov, J. Soures, and C. Stoeckl, Phys. Rev. Lett. **84**, 5153 (2000).
18. J. M. Foster *et al.*, Phys. Plasmas **9**, 2251 (2002).

19. J. A. Oertel *et al*., Rev. Sci. Instrum. **70**, 803 (1999).

20. R. L. Kauffman *et al*., Phys. Rev. Lett. **73**, 2320 (1994).

21. R. L. Kauffman *et al*., Rev. Sci. Instrum. **66**, 678 (1995).

22. H. N. Kornblum, R. L. Kauffman, and J. A. Smith, Rev. Sci. Instrum. **57**, 2179 (1986).

23. R. E. Olson *et al*., "Preheat Effects on Shock Propagation in Indirect-Drive Inertial Confinement Fusion Ablator Materials," to be published in Physical Review Letters.

24. R. E. Olson *et al*., "Shock Propagation, Preheat, and X-Ray Burn-through in NIF Ignition Capsule Ablator Materials," submitted to Physics of Plasmas.

25. A. Bar-Shalom *et al*., Phys. Rev. A **40**, 3183 (1989).

26. F. J. Rogers, B. G. Wilson, and C. A. Iglesias, Phys. Rev. A, Gen. Phys. **38**, 5007 (1988).

27. R. E. Olson *et al*., Rev. Sci. Instrum. **74**, 2186 (2003).

28. T. J. Orzechowski *et al*., Phys. Rev. Lett. **77**, 3545 (1996).

29. M. Houry *et al*., "A New Diagnostic Design to Achieve Neutron Spectroscopy in a High Gamma Background on ICF Experiments," presented at the EuroConference on Advanced Diagnostics for Magnetic and Inertial Fusion, Varenna, Italy, 3–7 September 2001.

30. Y. Giomataris *et al*., Nucl. Instrum. Methods Phys. Res. A **376**, 29 (1996).

31. D. C. Wilson *et al*., Nucl. Instrum. Methods Phys. Res. A **488**, 400 (2002).

32. G. J. Schmid, LLNL, private communication (2002).